Title

Coupled modeling of non-isothermal multiphase flow, solute transport and reactive chemistry in porous and fractured media: 2. Model Applications

Author

Xu, Tianfu

Publication Date

1998-09-01

LBNL-42051
Preprint

ERNEST ORLANDO LAWRENCE
BERKELEY NATIONAL LABORATORY

Coupled Modeling of Non-Isothermal Multi-Phase Flow, Solute Transport and Reactive Chemistry in Porous and Fractured Media: 2. Model Applications

Tianfu Xu, Eric Sonnenthal, Nicolas Spycher,
Karsten Pruess, and George Brimhall

Earth Sciences Division

September 1998

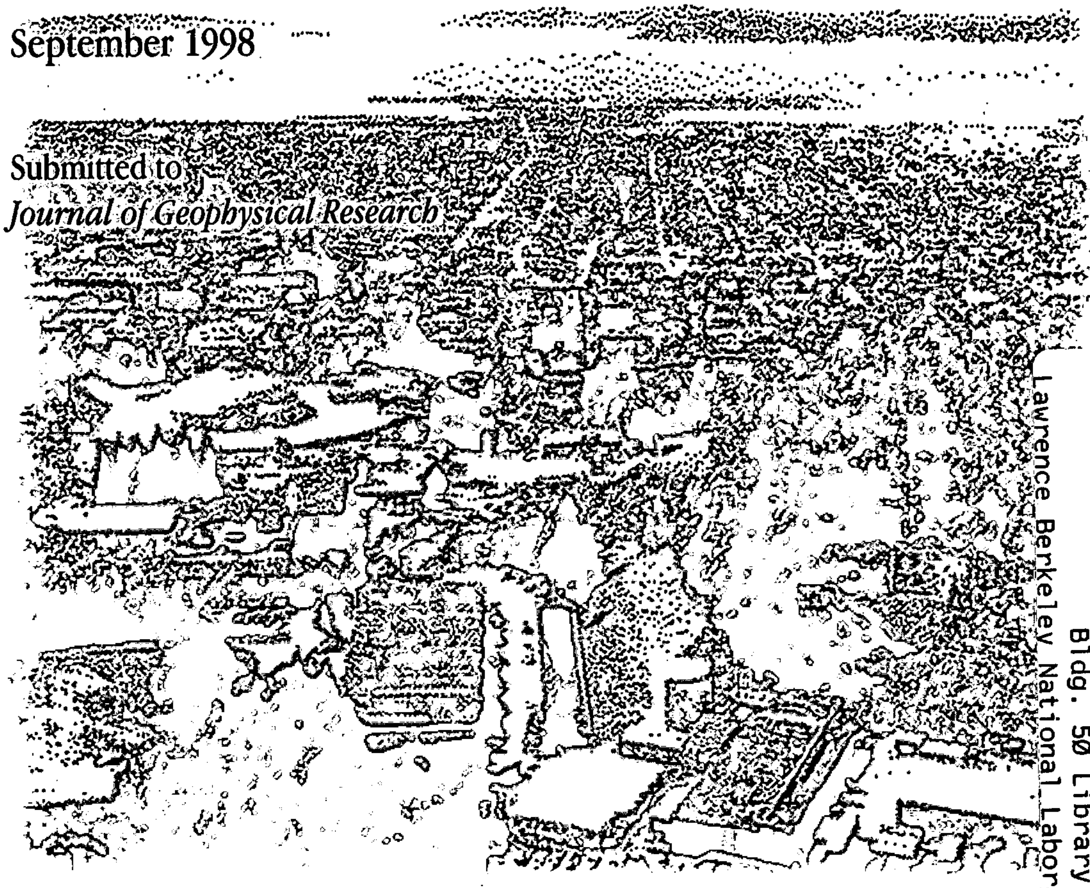

Submitted to
Journal of Geophysical Research

DISCLAIMER

LBNL-42051

Coupled Modeling of Non-Isothermal Multi-Phase Flow, Solute Transport and Reactive Chemistry in Porous and Fractured Media: 2. Model Applications

Tianfu Xu,[1] Eric Sonnenthal,[1] Nicolas Spycher,[1]
Karsten Pruess,[1] and George Brimhall[2]

[1]Earth Sciences Division
Ernest Orlando Lawrence Berkeley National Laboratory
University of California
Berkeley, California 94720

[2]Department of Geology and Geophysics
University of California
Berkeley, California 94720

September 1998

This work was supported by the Laboratory Directed Research and Development Program of the Ernest Orlando Lawrence Berkeley National Laboratory, under Contract No. DE-AC03-76SF00098 with the U.S. Department of Energy; and by the Director, Office of Civilian Radioactive Waste Management, U.S. Department of Energy, through Memorandum Purchase Order EA9013MC5X between TRW Environmental Systems Inc., and the Ernest Orlando Lawrence Berkeley National Laboratory.

Coupled modeling of non-isothermal multiphase flow, solute transport and reactive chemistry in porous and fractured media:

2. Model applications

Tianfu Xu[1], Eric Sonnenthal[1], Nicolas Spycher[1], Karsten Pruess[1] and George Brimhall[2]

[1] Earth Sciences Division, Lawrence Berkeley National Laboratory, University of California, Berkeley, CA 94720.

[2] Department of Geology and Geophysics, University of California at Berkeley.

Abstract. A comprehensive coupled model, TOUGHREACT, for non-isothermal multiphase flow, solute transport, and reactive chemistry has been presented in Part 1 of this two-part paper [this issue]. To demonstrate the model capabilities, here we present three applications. The first deals with the oxidative weathering of pyrite (FeS_2) and chalcopyrite ($CuFeS_2$) and associated acidification that causes mobilization of metals in the unsaturated zone, with subsequent formation of enriched ore deposits in the reducing conditions below water table. Redox reactions pose difficult challenges for numerical modeling for this problem because concentrations of some aqueous species involved may vary by tens of orders of magnitude. The second application consists of predicting thermal, hydrological, and chemical processes induced by emplacement of a strong heat source in unsaturated fractured rocks to simulate a high-level nuclear waste repository. Preliminary modeling results indicate that the importance of considering hydrochemical interactions between fracture and matrix for this type of system, such as the effect of CO_2 volatilization from matrix pore water and condensation in fractures. The simulations are also

useful to investigate mineral dissolution and precipitation patterns and their effect on the porosity of the host rock. The third example is the simulation of chemical evolution in an irrigated soil, to demonstrate flow and transport under ambient conditions in unsaturated porous media.

1. Introduction

A general coupled model, TOUGHREACT, which considers non-isothermal transport of multi-component chemical species in both liquid and gas phases, has been presented in Part 1 of this two-part paper [this issue]. A wide range of subsurface thermo-physical-chemical processes are considered. The code can be applied to one-, two-, or three-dimensional porous and fractured media with physical and chemical heterogeneity. To demonstrate the capabilities of TOUGHREACT to deal with a variety of reactive chemical transport problems, here we present three applications.

The first simulates supergene copper enrichment, the oxidative weathering of pyrite (FeS_2) and chalcopyrite ($CuFeS_2$) and associated acidification that causes mobilization of metals in the unsaturated zone, with subsequent formation of enriched ore deposits in the reducing conditions below the water table. Oxygen is supplied to a protore containing pyrite and chalcopyrite as a dissolved species in infiltrating rainwaters, and by gaseous diffusion from the land surface boundary. As aqueous phase oxygen is depleted through redox reaction, additional oxygen dissolves from the gas phase. Redox reactions pose difficult challenges for numerical modeling for this problem because concentrations of some aqueous species involved may vary by tens orders of magnitude. Because pyrite is a common mineral present in many hydrogeological systems, this problem has broad significance for geoscientific, engineering, and environmental applications.

The second application deals with simulating a thermal test currently underway for a proposed high-level nuclear waste repository. The purpose of the test and its modeling is to gain a better understanding of the coupled chemical, thermal, and hydrological processes that take place in an unsaturated fractured rocks following thermal loading by emplacement of a strong heat source. Modeling studies are used to predict mineral dissolution/precipitation and effects on porosity of the host rock.

The third example is the simulation of chemical evolution in an irrigated soil, to demonstrate the model capabilities to deal with flow and reactive transport under ambient conditions in unsaturated porous media. Variations of CO_2 gas partial pressure play an important role in chemical evolution for unsaturated soils [Domenico et al., 1990]. Calcite dissolution-precipitation and cation exchange are also considered, which are significant for the soil-water interaction.

2. Supergene copper enrichment

2.1. Problem statement

Oxidative weathering processes of sulfide minerals such as pyrite (FeS_2) and chalcopyrite ($CuFeS_2$) in unsaturated zones is very significant for assessment and recovery of metal ore deposits and acid mine drainage problems. Supergene copper enrichment involves the oxidative weathering and acidification that causes mobilization of metals in the unsaturated zone, with subsequent formation of enriched ore deposits in the reducing conditions below the water table. Such redox-driven processes have produced some of the world's largest copper deposits [*Ague and Brimhall*, 1989]. The geochemistry for this application was based on field and laboratory studies of supergene copper systems and their dynamics under conditions of climatic change as carried out by *Brimhall et al* [1985], and *Ague and Brimhall* [1989]. We first consider the supergene copper enrichment in a one-dimensional unsaturated-saturated porous medium. Then the case in a two-dimensional fractured porous medium is presented.

2.2. One-dimensional porous medium

A schematic representation of the model system is shown in Figure 2.1. Oxygen is supplied to a protore containing pyrite and chalcopyrite (Table 2.1) as a dissolved species in infiltrating rainwaters, as well as by gaseous diffusion from the land surface boundary. A vertical column of 20 m thickness is used, which is discretized into 10 grid blocks with a constant spacing of 2 m. The top 5 blocks represent the unsaturated zone (water saturation: 0.43, 0.43, 0.44, 0.48 , 0.72 from the top to the bottom), while the bottom 5 blocks represent the water saturated zone. A steady-state water flow regime is assumed throughout; mineral dissolution/precipitation effects on porosity and permeability are not considered in the current simulation. A gaseous diffusion coefficient of 4.38×10^{-5} m^2s^{-1} is used. The tortuosity for gaseous oxygen diffusion, τ_g, is computed from the *Millington and Quirk* [1961] model, $\tau_g = \phi^{1/3}S_g^{7/3}$, where ϕ is the medium porosity, and S_g is the gas phase saturation.

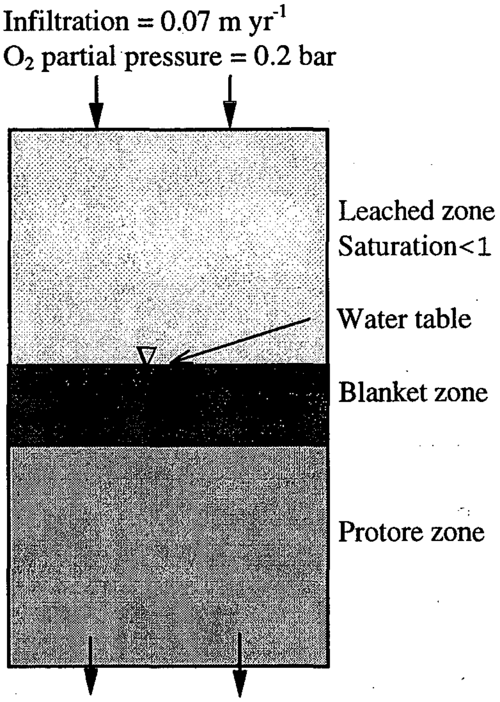

Figure 2.1. Schematic representation of a one-dimensional supergene copper enrichment system

The column is initially filled entirely with a protore mineral assemblage as listed in Table 2.1. The dissolution of the protore minerals is kinetically controlled. We use the rate expression given in Table 3 of Part 1 of this two-part paper [this issue]. The kinetic rate constants and specific surface areas used are also given in Table 2.1. The chemical formulae and dissociation stoichiometries of the primary minerals are given in Table 2.2. Oxygen is treated as an ideal gas, and its interaction with the aqueous solution is assumed at equilibrium. The precipitation of secondary minerals (Table 2.3) during the simulation progress is also assumed to proceed at equilibrium.

Table 2.1. Chemical properties of protore mineral reactants. Volume fraction, rate constant and specific surface area are based on *Ague and Brimhall* [1989] and *Gerard et al.* [1997]. Abundance is calculated from volume fractions (in this table) and molar volumes presented in the EQ3/6 database [*Wolery*, 1992].

Mineral	Volume fraction (%)	Abundance (mol/dm^3 medium)	Rate constant (mol/cm^2/s)	Surface area (cm^2/dm^3 medium)
Pyrite	9.0	3.76	4.0×10^{-15}	586.7
Chalcopyrite	4.5	1.05	4.0×10^{-15}	586.7
Magnetite	4.5	1.01	2.0×10^{-15}	586.7
K-feldspar	18.0	1.65	3.1×10^{-16}	5866.7
Albite	9.0	0.9	3.1×10^{-16}	6981.3
Anorthite	9.0	0.89	1.5×10^{-16}	2992.0
Annite	4.5	0.29	2.4×10^{-18}	2933.3
Muscovite	9.0	0.64	2.4×10^{-18}	1760.0
Quartz	18.0	7.93	4.3×10^{-18}	6160.0
Anhydrite	4.5	0.98	1.5×10^{-16}	586.7
	Total=90			
	Void=10			

Table 2.2. Chemical reactions for oxygen gas and the primary mineral reactants. The thermodynamic equilibrium constants are from the EQ3/6 database [*Wolery*, 1992]

Mineral (or gas)	Reactions equation	log K (25°C)
Oxygen gas	$O_2(g) = O_2(aq)$	-2.898
Pyrite	$FeS_2 + H_2O + 3.5O_2(aq) = 2SO_4^{--} + Fe^{++} + 2H^+$	217.4
Chalcopyrite	$CuFeS_2 + 4O_2(aq) = 2SO_4^{--} + Fe^{++} + Cu^{++}$	244.07
Magnetite	$Fe_3O_4 + 8H^+ = Fe^{++} + 2Fe^{+++} + 4H_2O$	10.4724
K-feldspar	$KAlSi_3O_8 + 4H^+ = K^+ + Al^{+++} + 3\ SiO_2(aq) + 2H_2O$	-0.2753
Albite	$NaAlSi_3O_8 + 4H^+ = Na^+ + Al^{+++} + 3\ SiO_2(aq) + 2H_2O$	2.7645
Anorthite	$CaAl_2Si_2O_8 + 8H^+ = Ca^{++} + 2Al^{+++} + 2\ SiO_2(aq) + 4H_2O$	26.5780
Annite	$KFe_3AlSi_3O_{10}(OH)_2 + 10H^+ = K^+ + 3Fe^{++} + Al^{+++} + 3\ SiO_2(aq) + 6H_2O$	29.4693
Muscovite	$KAl_3Si_3O_{10}(OH)_2 + 10H^+ = K^+ + 3Al^{+++} + 3\ SiO_2(aq) + 6H_2O$	13.5858
Quartz	$SiO_2 = SiO_2(aq)$	-3.9993
Anhydrite	$CaSO_4 = Ca^{++} + SO_4^{--}$	-4.3064

Table 2.3. The chemical reactions for secondary minerals. The thermodynamic equilibrium constants are from the EQ3/6 database [*Wolery*, 1992]

Mineral	Reaction equation	log K (25°C)
Covellite	$CuS + H^+ = Cu^{++} + HS^-$	22.8310
Chalcocite	$Cu_2S + H^+ = 2Cu^+ + HS^-$	-34.7342
Bornite	$Cu_5FeS_4 + 4H^+ = Cu^{++} + 4Cu^+ + Fe^{++} + 4HS^-$	-102.44
Goethite	$FeOOH + 3H^+ = Fe^{+++} + 2H_2O$	-0.283
Hematite	$Fe_2O_3 + 6H^+ = 2Fe^{+++} + 3H_2O$	0.1086
Kaolinite	$Al_2Si_2O_5(OH)_4 + 6H^+ = 2Al^{+++} + 2\ SiO_2(aq) + 5H_2O$	6.8101
Alunite	$KAl_3(OH)_6(SO_4)_2 + 6H^+ = K^+ + 3Al^{+++} + 2SO_4^{--} + 6H_2O$	-0.3479
Amorphous silica	$SiO_2 = SiO_2(aq)$	-2.7136

A dilute oxidizing water with an oxygen partial pressure of 0.2 bar is initially placed in the five uppermost (unsaturated) grid blocks, while a reducing water with a oxygen partial pressure of 1.0×10^{-70} bar is assumed for the remaining (saturated) grid blocks. The infiltration water composition is the same as the initial unsaturated water. A total of 52 aqueous species are considered (Table 2.4). The aqueous complexation is assumed at equilibrium. Detailed results for the chemical evolution, simulated with TOUGHREACT, are given in Figures 2.2 and 2.3.

Table 2.4. Aqueous species considered in the TOUGHREACT simulations of supergene copper enrichment. Secondary species can be expressed in terms of the primary species.

Primary species:

H^+
H2O
O_2(aq)
SO_4^{--}
Fe^{++}
Cu^{++}
Na^+
K^+
Ca^{++}
Al^{+++}
SIO_2(aq)
Cl^-

Secondary species:

OH^-
HSO_4^-
H_2SO_4(aq)
$NaSO_4^-$
KSO_4^-
$CaSO_4$(aq)
$FeSO_4$(aq)
$Fe(SO_4)_2^-$
$FeSO_4^+$
$FeCl^+$
$AlSO_4^+$
$Al(SO_4)_2^-$
$AlOH^{++}$
$Al(OH)_2^+$
$Al_2(OH)_2^{+4}$
$Al_3(OH)_4^{+5}$
$HAlO_2$(aq)
AlO_2^-
$FeCl^{++}$
$FeCl_2^+$
$FeOH^+$
$FeOH^{++}$
$Fe(OH)_2^+$
$Fe_2(OH)_2^{+4}$
$Fe(OH)_2$(aq)
$Fe(OH)_3$(aq)
$Fe_3(OH)_4^{+5}$
$CaOH^+$
Cu^+
$CuOH^+$
$CuCl_2$(aq)
$CuCl_2^-$
$CuCl_4^{--}$
$CaCl^+$
KCl(aq)
Fe^{+++}
HS^-
H_2S(aq)
$HSiO_3^-$
$NaHSiO_3$(aq)

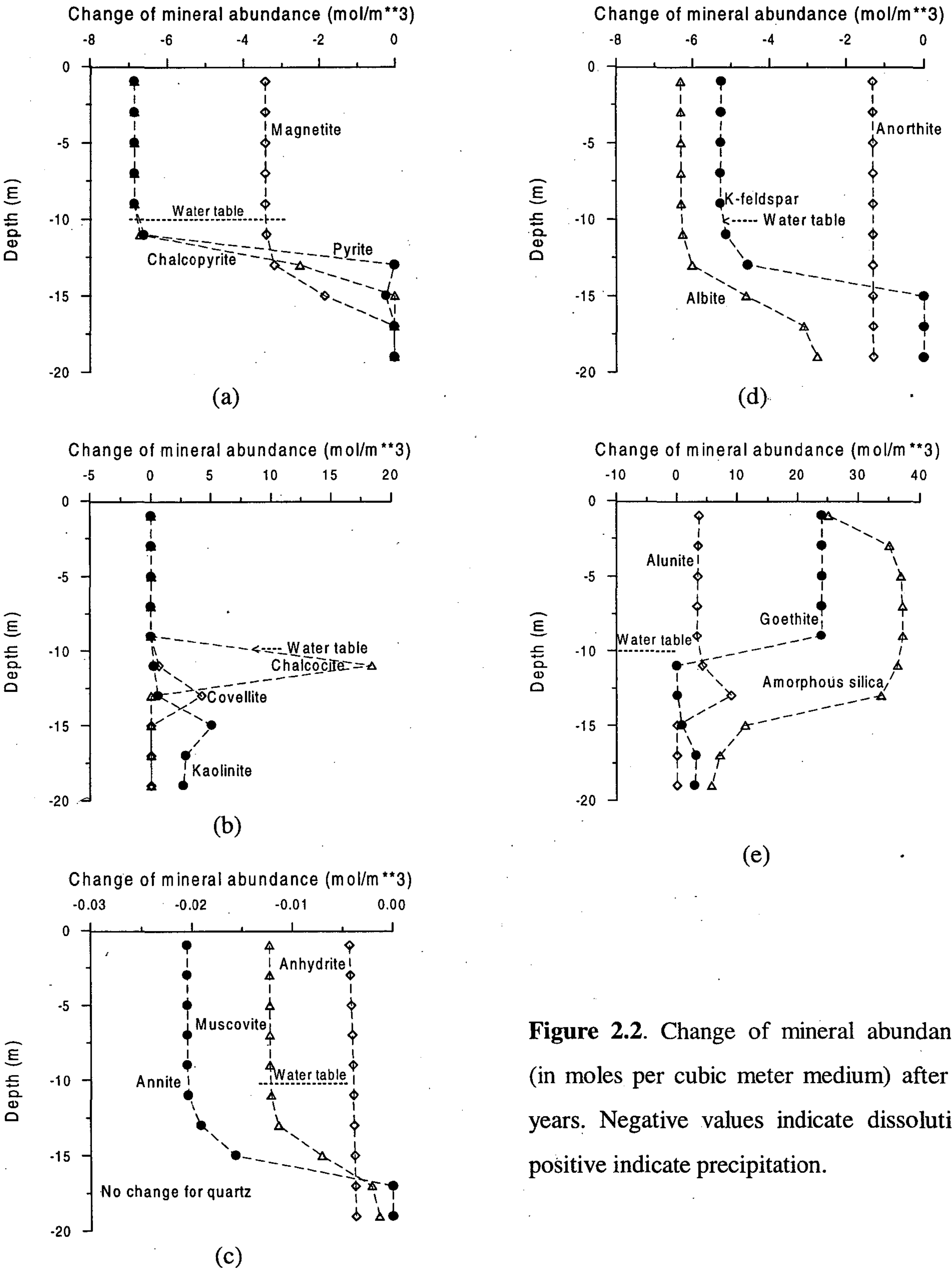

Figure 2.2. Change of mineral abundances (in moles per cubic meter medium) after 90 years. Negative values indicate dissolution, positive indicate precipitation.

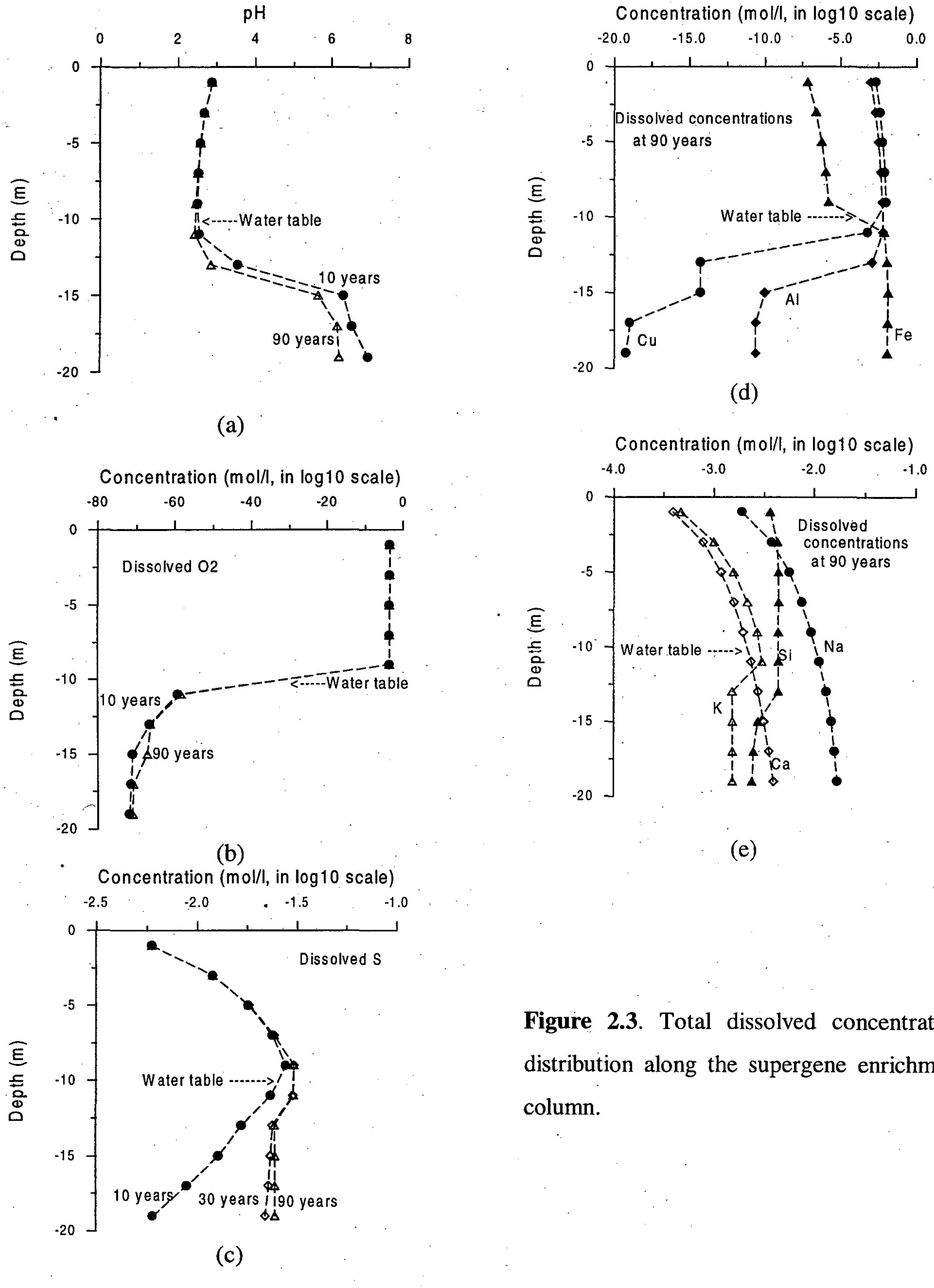

Figure 2.3. Total dissolved concentration distribution along the supergene enrichment column.

In the unsaturated zone, pyrite and chalcopyrite are oxidized and dissolved (Figure 2.2a). As aqueous phase oxygen is depleted through reaction with pyrite and chalcopyrite, it is replenished by dissolution from the gas phase, and by diffusive oxygen gas transport from the atmospheric boundary at the land surface. The pH decreases downward (Figure 2.3a), and the total dissolved Cu and S concentrations increase (Figures 2.3c and 2.3d) due to pyrite and chalcopyrite oxidation. When the downward-percolating aqueous solution reaches the reducing saturated zone, the secondary copper bearing minerals chalcocite and covellite are precipitated (Figure 2.2b), forming the enrichment blanket immediately below the water table [*Ague and Brimhall*, 1989]. In addition, goethite precipitates in the unsaturated zone.

At the same time magnetite, K-feldspar, albite, anorthite, annite and muscovite dissolve throughout the column due to the pH decrease (Figures 2.2a, c and d). Magnetite dissolution (Figure 2.2a) creates additional Fe^{2+} and Fe^{3+}. Fe^{3+} also acts as an oxidant, which contributes to pyrite and chalcopyrite oxidation. Dissolution of K-feldspar, albite, anorthite, annite and muscovite produces Na, K, Ca, Al and SiO_2(aq). As a result, amorphous silica precipitates throughout the column (Figure 2.2e). Kaolinite precipitates only in the bottom 3 grid blocks of the saturated zone (Figure 2.2b), while alunite appears only in the top 7 grid blocks of the column (Figure 2.2e). There is no quartz dissolution as this mineral is stable in our simulation, as it is in nature.

The chemical changes and secondary mineral assemblages predicted by our model are consistent with observations in supergene copper deposits in the Atacama Desert, Northern Chile [*Ague and Brimhall*, 1989].

2.3. Two-dimensional fractured porous medium

Supergene copper enrichment normally took place in a fractured porous medium [such as El Salvador, Chile; *Ague and Brimhall*, 1989]. The method of "multiple interacting continua" [MINC; *Pruess and Narasimhan*, 1985] is here employed to resolve "global" flow and diffusion of chemicals in the fracture system, and its interaction with "local" exchange between fracture and matrix rock. The resolution for a matrix block is achieved by appropriate subgridding, as shown in Figure 2.4. The MINC concept is based on the notion that changes in fluid pressures and chemical concentrations will propagate rapidly through the fracture system, while invading the tight matrix blocks only slowly. Therefore, changes in matrix conditions will be (locally) controlled by the distance from the fractures, and can then be modeled by means of one-dimensional strings of nested grid blocks.

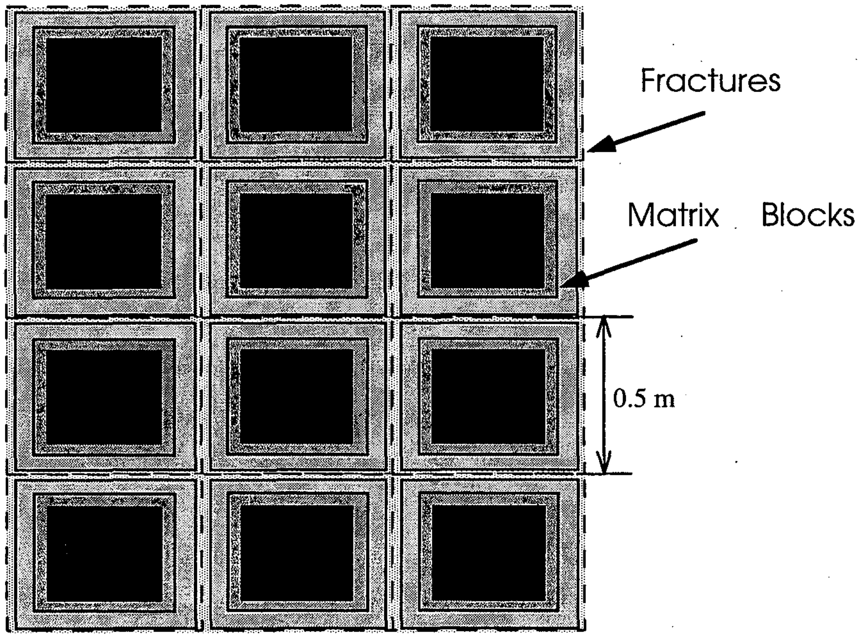

Figure 2.4. Subgridding in the method of "multiple interacting continua" (MINC). The figure represents an areal view of rock matrix columns that are separated by vertical fractures.

An idealized fractured porous medium with a set of equidistant, vertical fractures was used (see Figure 2.4; however, any fracture geometry can be considered by the MINC model). Because of symmetry only one column of matrix blocks needs to be modeled. The same rainwater infiltration rate as for the previous porous medium problem was used; all infiltration occurs in the fractures. Water pressure is held constant at 2 bar at the bottom (z = -20 m) and the water table is located at a depth of 10 m (Figure 2.5). The steady state water saturations obtained by ignoring chemical reactions are used as initial conditions for the calculation of reactive chemical transport. Hydrological parameters for the fracture and matrix are listed in Table 2.4. The other conditions are unchanged from the previous 1-D simulation.

Table 2.4. Hydrological parameters used for supergene copper enrichment in the fractured porous medium.

Parameter	Matrix	Fracture
Permeability (m^2)	10^{-16}	10^{-12}
Fracture domain volume fraction, v [*]		0.01
Fracture spacing (m)		0.5
Porosity	0.08	0.5^{**}
Relative permeability and capillary pressure (van Genuchten, 1980):		
λ	0.457	0.457
S_{lr}	0.1	0.05
S_{ls}	1.0	1.0
P_0(pa)	2.17×10^5	6.2×10^3

[*] $v = V_f/(V_f + V_m)$ where V_f and V_m are fracture and matrix domain volumes.

[**] Fracture domain is defined to include 50% by volume of wall rock.

The tight rock matrix is almost water saturated (see Figure 2.5), and oxygen access in the matrix is impeded. Pyrite and chalcopyrite oxidative dissolution takes place mostly in close proximity to the unsaturated fracture zone (see Figure 2.6). Away from the fracture zones, dissolution rates decrease. Chalcocite precipitation occurs mainly in the matrix just above the water table, and also in the deep fracture far below the water table (see Figure 2.7). A minor amount of covelite precipitates in the deep fracture (see Figure 2.8). The pattern of precipitation is different from the previous 1-D porous medium system. In the saturated zone, most water flow is passed through the fracture. The flux is much higher than in the previous case, so much more aqueous oxygen is available in the fracture and the oxidizing zone extends below the water table.

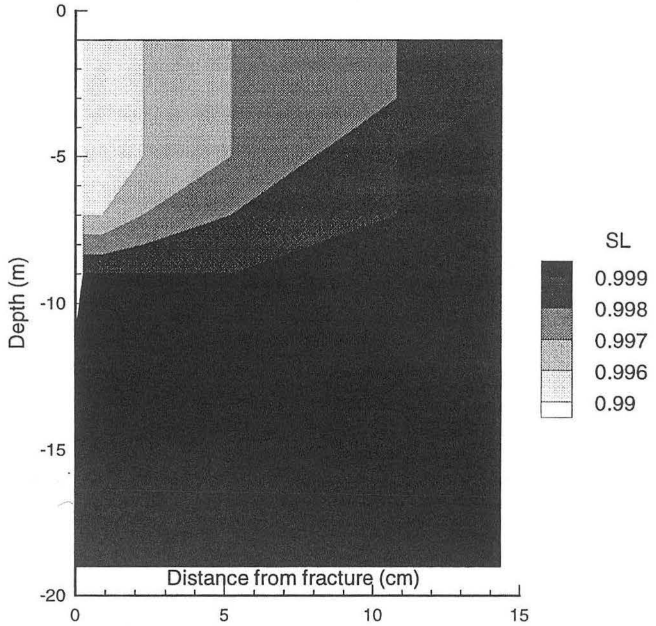

Figure 2.5. The steady-state water saturation for supergene copper enrichment in the fractured porous medium.

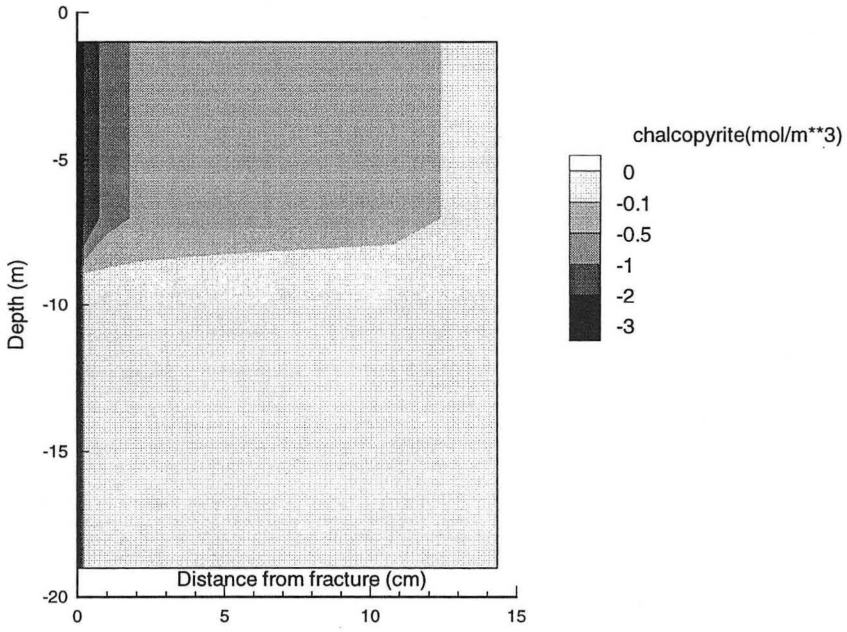

Figure 2.6. Change of chalcopyrite abundance (in moles per cubic meter medium) after 100 years. Note that change of pyrite abundance follows the same pattern.

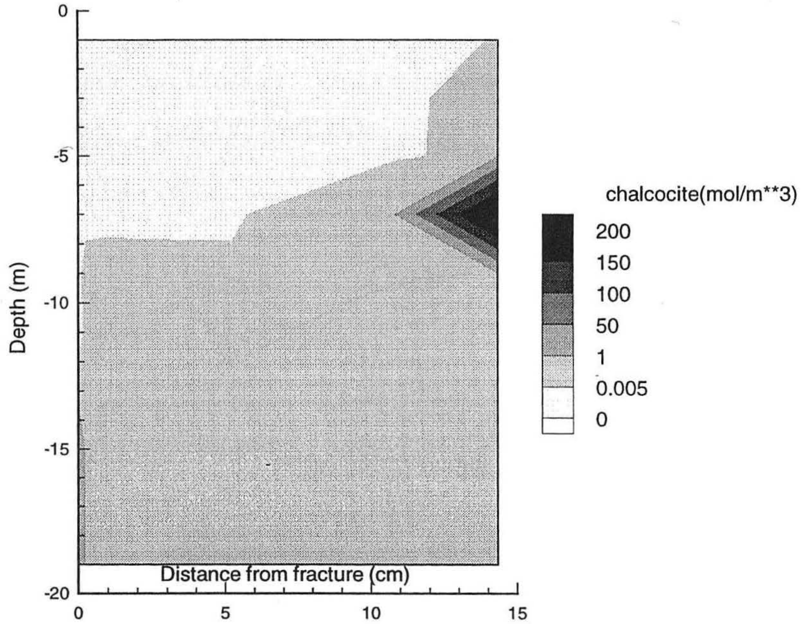

Figure 2.7. Change of chalcocite abundance (in moles per cubic meter medium) after 100 years.

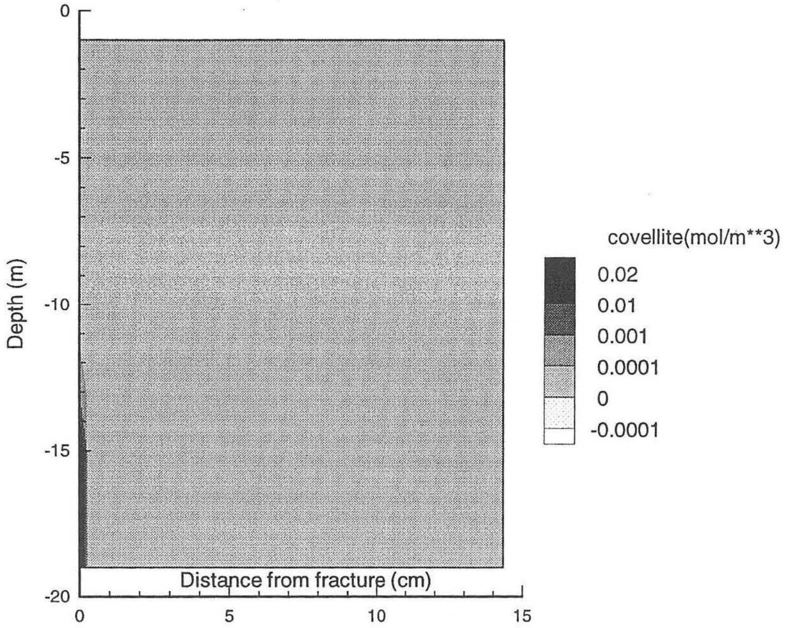

Figure 2.8. Change of covellite abundance (in moles per cubic meter medium) after 100 years.

2.4. Discussion

Oxidative weathering is an extremely difficult process to model numerically, because (1) it is driven by oxygen whose concentration in ambient soil gas, and dissolved in pore water in the unsaturated zone, is very small compared to the amounts of solid minerals which are to be reacted, and (2) the chemical activities and total elemental solubilities of key species vary over tens of orders of magnitude during redox processes. Our model provides a comprehensive suite of process modeling capabilities. The application to a supergene copper enrichment system demonstrated stable convergence behavior and geochemically reasonable results. This problem serves as a prototype for oxidative weathering processes with broad significance for geoscientific, engineering, and environmental applications.

3. Thermo-hydro-chemical modeling for the drift scale heater test at Yucca Mountain, Nevada

3.1 Problem statement

The Drift Scale Test (DST) is an underground thermal test currently underway at Yucca Mountain, Nevada. This test was designed to gain a better understanding of the coupled thermal, hydrological, chemical, and mechanical (THCM) processes which may take place around a heat-generating high-level nuclear waste repository. The test essentially consists of heating up the host rock (a welded tuff) through electric heaters located along a main 50-meter drift, and through a series of wing heaters. Many THCM parameters are monitored during this test. The test was begun in December, 1997 with a planned duration of eight years (four years of heating and four years of cooling). The maximum temperature during the test is expected to reach approximately 200 °C at the wall of the drift [*Birkholzer and Tsang*, 1997]. The preliminary simulations using TOUGHREACT were carried out to provide a pre-test analysis of the possible mineral alteration products and changes in pore-water and gas chemistry that could occur during the test. Several simulations have been performed. Here we present one of these simulations (DST-2). Results are preliminary and should not be used to infer the long-term behavior of a nuclear waste repository. The simulation is present only to illustrate the modeling of a complex thermal, hydrological, and chemical (THC) system. Further details are given in *Sonnenthal et al.* [1998].

Modeling of the thermohydrologic and chemical evolution of a unsaturated and fractured welded tuff at temperatures up to and above boiling presents numerous challenges in terms of conceptual model development and computer model application. There is a very large permeability contrast between the matrix of the welded tuff (approximately 10^{-17} m^2) and the fracture system (10^{-13} m^2). This results in very different velocities of vapor and liquid flow in the two media, as well as different processes, such as boiling in the matrix with vapor discharge into the fractures, and condensation in cooler portions of the fractures followed by water imbibition in to the matrix. Another challenge is posed by the differences in mineralogy between matrix and fractures of the welded tuff. For example, calcite, opal, and zeolites are abundant in fractures, but are much less common in the matrix [*Paces et al.*, 1998]. In addition, changes in dissociation constants and reaction rates with temperature result in changing geochemical behavior as the system heats up and cools down, making the numerical simulation difficult.

3.2. Approach and model parameters

The disparity in transport processes and mineralogy between fractures and matrix necessitates the use of an approach that can capture the significant gradients of temperature, water saturation, and chemical concentrations between the two media. For this modeling effort we chose the dual permeability method. Although it only has a limited ability to resolve gradients (of temperature, water saturation, and chemical concentrations) between fractures and matrix rock, the dual permeability method is a substantial improvement over single continuum or equivalent continuum methods for such highly transient problems.

Prior to modeling the chemical evolution of the DST, a detailed predictive analysis of the thermohydrology of the DST was carried out by *Birkholzer and Tsang* [1997], which was updated after six months of heating [*Birkholzer and Tsang*, 1998]. For the modeling work presented here, simulations were performed on two-dimensional vertical cross-sections. The dual permeability numerical mesh (Figure 3.1a) has 2242 grid blocks for each of the fracture and matrix continua. Boundary and initial conditions, and thermohydrologic properties of the welded tuffs were taken from *Birkholzer and Tsang* [1997]. A close-up view of the mesh around the heated areas is shown in Figure 3.1b.

During the relatively short period (eight years) of the thermal test, chemical evolution is controlled mainly by temperature change. The effect of infiltration on chemical evolution can be neglected because it is very small (on the orders of a few millimeters per year). The inside wall of the heater drift is considered to be a no-flux boundary for water, vapor, and aqueous and gaseous species. The heating schedule is the base case presented by *Birkholzer and Tsang* [1997] with 100% output for the first year, 50% for the following 3 years, followed by a cool down period of 4 years.

The initial water composition used in the TOUGHREACT simulation is presented in Table 3.1. Aqueous species considered in calculations are listed in Table 3.2. The interaction of CO_2 gas with the aqueous solution are assumed at equilibrium. Initial mineral volume fractions, possible secondary mineral phases considered, and reaction rate law parameters used are presented in Table 3.3. The aqueous species diffusion coefficient was assumed to be 1×10^{-9} m^2/s in matrix and fractures. The tortuosity was set to 0.2 in fractures and matrix. The diffusion coefficient for CO_2 in the gas phase was set to 1×10^{-7} m^2/s [*Moridis and Apps*, 1997].

Table 3.1. Initial pore and fracture water composition used in preliminary simulation DST-2 for The Drift-Scale-Heater Test at Yucca Mountain, Nevada [*Sonnenthal et al.*, 1998]. These values are average of water sample data from wells UZ-16, DS-9 and SD-12 [*Yang*, 1996].

	Concentration (mg/L)
Ca^{2+}	27
Mg^{2+}	5
Na^{+}	91
HCO_3^{-}	219^{*}
Cl^{-}	41
SO_4^{2-}	40
SiO_2	60
Al	$1\times10^{-6\,**}$
K	4^{**}
pH	8.2

* Adjusted for charge balance

** Estimated

Table 3.2. Aqueous species considered in simulation DST-2 for The Drift-Scale-Heater Test at Yucca Mountain, Nevada

Primary species	Secondary species	
H_2O	$CO_2(aq)$	CO_3^{2-}
H^+	OH^-	Al^{3+}
Ca^{2+}	$Al(OH)_2^+$	$HAlO_2$
Mg^{2+}	$AlOH^{2+}$	$CaCl^+$
Na^+	$CaCl_2(aq)$	$CaCO_3(aq)$
K^+	$CaHCO_3^+$	$CaSO_4(aq)$
$SiO_2(aq)$	$HSiO_3^-$	$HCl(aq)$
HCO_3^-	$KCl(aq)$	$KHSO_4(aq)$
SO_4^{2-}	KSO_4^-	$MgCl^+$
Cl^-	$MgCO_3(aq)$	$MgHCO_3^+$
AlO_2^-	$MgSO_4(aq)$	$NaCl(aq)$
Sr^{2+}	$NaCO_3^-$	$NaHCO_3(aq)$
$^{86}Sr^{2+}$	$NaHSiO_3$	$SrCl^+$
	$SrCO_3(aq)$	$^{86}SrCl^+$
	$^{86}SrCO_3(aq)$	

Table 3.3. Initial mineral volume fractions (V_f) and possible secondary mineral phases ($V_f = 0.0$) considered in simulation DST-2 [*Sonnenthal et al.*, 1998]. Reaction rate law parameters (precipitation and dissolution) are from *Johnson et al.* [1998], *Hardin* [1998], and *Tester et al.* [1994] or estimated from these data. The rate constant k is calculated from, $k = k_0 \exp[-E_a / R(1/T - 1/298.15)]$, where R is the gas constant and T is absolute temperature [*Aagaard and Helgeson*, 1982]. Calcite and anhydrite are considered equilibrium minerals.

Minerals	V_f (matrix)	V_f (fractures)	k_0 (mol/m^2s)	E_a (kJ/mol)	Surface area (m^2/kgH_2O)
Quartz	0.1018	0.0995	1.2589×10^{-14}	87.5	71.07
Cristobalite-a	0.2292	0.2241	3.1623×10^{-13}	69.08	71.07
Am. SiO_2 *	0.0	0.0	7.944×10^{-13}	62.8	142.14
Calcite	0.0	0.02	at equilibrium		
Anhydrite	0.0	0.0	at equilibrium		
Microcline	0.3009	0.2942	1.0×10^{-12}	57.78	142.4
Albite-low	0.2498	0.2441	1.0×10^{-12}	67.83	104.2
Anorthite (Sr)	0.0083	0.0087	1.0×10^{-12}	67.83	124.6
Kaolinite	0.0	0.0	1.0×10^{-13}	62.80	142.4
Illite	0.0	0.005	1.0×10^{-14}	58.62	142.4
Sepiolite	0.0	0.0	1.0×10^{-14}	58.62	142.4
Smectite-Na	0.0	0.0	1.0×10^{-14}	58.62	142.4
Smectite-K	0.0	0.0	1.0×10^{-14}	58.62	142.4
Smectite-Ca	0.0	0.0	1.0×10^{-14}	58.62	142.4
Smectite-Mg	0.0	0.0	1.0×10^{-14}	58.62	142.4

* Precipitation rate law from Rimstidt and Barnes (1980): $\log k = -7.07 - 2598/T(K)$. Reactive surface area for amorphous silica is assumed twice that of the other silica phases. All other kinetic minerals were given the same rate law for precipitation as dissolution, except quartz and cristobalite for which precipitation was suppressed.

The extent of strontium isotopic fractionation in pore waters by dissolution of feldspar (anorthite endmember) was simulated by replacing a small amount of Ca by ^{86}Sr and a related component Sr', from which the $^{87}Sr/^{86}Sr$ in the pore fluid can be calculated [*Sonnenthal et al.*, 1998], as follows:

$$^{87}\mathrm{Sr}/^{86}\mathrm{Sr} = \frac{\mathrm{Sr}'}{^{86}\mathrm{Sr}} - 1 \tag{3.1}$$

where

$$\mathrm{Sr}' = \mathrm{Sr}_{\mathrm{total}}[1 - (^{84}\mathrm{Sr} + ^{88}\mathrm{Sr})] \tag{3.2}$$

This relation assumes that there is no radioactive decay of ^{87}Rb to ^{87}Sr and that the masses of the different Sr isotopes are identical. The proportions of ^{84}Sr and ^{88}Sr are also assumed constant (^{84}Sr = 0.0056, ^{88}Sr = 0.8253; Faure, 1977).

3.3. Simulation results

During the initial heating stage, rocks are heated significantly above the boiling point, and evaporation and boiling of pore waters takes place. The area closest to the heat source eventually dries up, giving rise to a dryout zone, which is surrounded by a boiling zone. A condensation zone develops beyond the volume of rock in which boiling takes place, in which CO_2 is uptaked from the vapor phase. Condensation occurs primarily in fractures and leads to liquid saturation increase and subsequent drainage in fractures, mostly towards areas below the heat source. These processes are illustrated by the simulation results presented below.

Computed partial pressures of CO_2 (P_{CO2}) in fractures are shown in Figure 3.2, indicating extremely low values in the dryout zone at the wing heaters and near the heater drift wall. The availability of CO_2 by diffusion can affect the magnitude of this reduction in CO_2 partial pressure; however, sensitivity studies from a maximum diffusivity of 1×10^{-5} m^2/s to zero have shown the P_{CO2} to decrease at all these diffusivity values, yet to a somewhat lesser degree at higher diffusivities. Fracture pore water pH (Figure 3.3) is shifted to high values (near 10 in the condensation zone, and extreme values above 11 in the dryout/boiling zone). Changes (in volume fraction) of cristobalite, K-feldspar, albite, anorthite and kaolinite due to precipitation and dissolution in fractures are presented in Figures 3.4 through 3.8.

To help in understanding the chemical reaction dynamics, profiles of the pore-water chemistry, changes of mineral abundance, temperature, and water saturation were plotted for a vertical section through the wing heater at approximately 12 meter to the left of the heater drift (Figures 3.9 and 3.10).

The most noticeable feature in this simulation is the high pH in the remaining water just prior to dryout (mostly above 8.5 and up to 11 or more). The pH increase is attributed to CO_2 degassing due to the temperature increase

$$HCO_3^- + H^+ \rightarrow CO_2\,(g) + H_2O \qquad (3.3)$$

This pH increase, together with the temperature increase, leads to the precipitation of calcite (which has a retrograde solubility):

$$Ca^{2+} + HCO_3^- \rightarrow CaCO_3\,(\text{calcite}) + H^+ \qquad (3.4)$$

The other reaction which contributes to pH increase is the conversion of anorthite to kaolinite, which can be combined with the precipitation of calcite as follows:

$$CaAl_2Si_2O_8 \text{ (anorthite)} + H_2O + HCO_3^- + H^+ \rightarrow$$
$$Al_2Si_2O_5(OH)_4 \text{ (kaolinite)} + CaCO_3 \text{ (calcite)} \qquad (3.5)$$

This reaction has a strong forward equilibrium constant. However, the this equilibrium constant decreases with temperature and therefore the extent of this reaction would be expected to decrease with temperature. This is not the case, as shown on Figure 3.10, where a clear one-to-one correspondence can be observed between anorthite dissolution and kaolinite precipitation as the temperature increases. Therefore, it appears that this reaction is driven by kinetic rates that do not reflect trends at equilibrium. Because of the elevated pH, it is likely that a phase other than kaolinite would prevail, such as a zeolite. Whether this reaction actually takes place is uncertain at this time and will be assessed though monitoring of the DST and additional simulations with other mineral phases.

Examination of Figures 3.9 and 3.10 yields further insight into water-rock interaction processes as one moves closer to the wing heater. At about 3 meters from the heater, the total carbonate concentration in water starts to drop significantly through CO_2 degassing and calcite precipitation. At 2 meters from the heater, the parallel and decreasing trends of chloride, sulfate and sodium clearly indicate dilution from vapor condensation. This condensation is accompanied by CO_2 dissolution and causes the pH to drop more than 1 unit, which together with dilution further drives reaction (3.5) and precipitates kaolinite, this time from dissolution of anorthite as well as of albite:

$$2NaAlSi_3O_8 \text{ (albite)} + H_2O + 2H^+ \Rightarrow$$
$$Al_2Si_2O_5(OH)_4 \text{ (kaolinite)} + 4SiO_2(aq) + 2Na^+ \qquad (3.6)$$

The slightly higher amount of condensation below the heater (left sides of Figures 3.9 and 3.10) when compared to above the heater (right sides) results in a decrease in calcite precipitation and slight increase in albite dissolution that are more pronounced below the heater than above it. The boiling zone is very narrow on each side of the thin dry-out zone after 2 months (less than half a meter). Boiling induces a sharp reversal of reactions (3.5) and (3.6) due to further pH increase by the now extreme CO_2 depletion. Anhydrite forms under extreme dryout conditions.

Pore water strontium isotopic ratios show a shift to about 0.716 to 0.718 (see Figure 3.11) where there is significant feldspar dissolution (anorthite component). This effect would be reduced by any calcite dissolution (with an isotopic ratio close to that of the initial pore water) that was not included in the model; however the modeled shift suggests that the effective dissolution rates of feldspar in the simulation are significant enough to shift the isotopic ratio of the pore waters. Whether these effective dissolution rates are reasonable will be assessed by monitoring of the pore water chemistry, and by the isotopic ratio and total Sr content of any collected condensate waters.

3.4. Discussion

This study reveals that the transport dynamics (advection and diffusion) of CO_2 in the gas phase, the mineral assemblage, and the thermodynamic and kinetic parameters considered in the model are crucial in controlling the system pH, pore water chemistry, and overall rates of reaction. Many parameters used in these exploratory simulations are currently quite uncertain.

Volumetrically the most important reactions are strong dissolution of cristobalite and variable amounts of calcite precipitation in fractures. Amorphous silica and anhydrite precipitate in the dryout regions, but high pH causes an increase in silica solubility. Feldspar dissolution is also quite strong. The rates of reaction used in this study are likely overestimated and not representative of field conditions, especially when considering the possibility of mineral coatings reducing the reactive surface area. The rates of plagioclase dissolution (albite + anorthite) should result in a significant shift in the strontium isotopic ratio if the anorthite component is dissolving as strongly as predicted by the simulation. This will be easily tested by analyzing condensate waters for strontium isotopic ratios, allowing a further constraint on the effective reaction rates.

The dual permeability model provides a suitable framework that captures the essential physical and chemical aspects of fractured porous media; although a more refined discretization such as MINC [*Pruess and Narasimhan*, 1985] could resolve concentration and mineralogical gradients more accurately. The dual permeability model is also critical to evaluate realistically chemical interactions in a boiling fractured system, where CO_2 volatilization from matrix pore water and condensation in fractures play an important role in controlling pH and mineral dissolution and precipitation patterns.

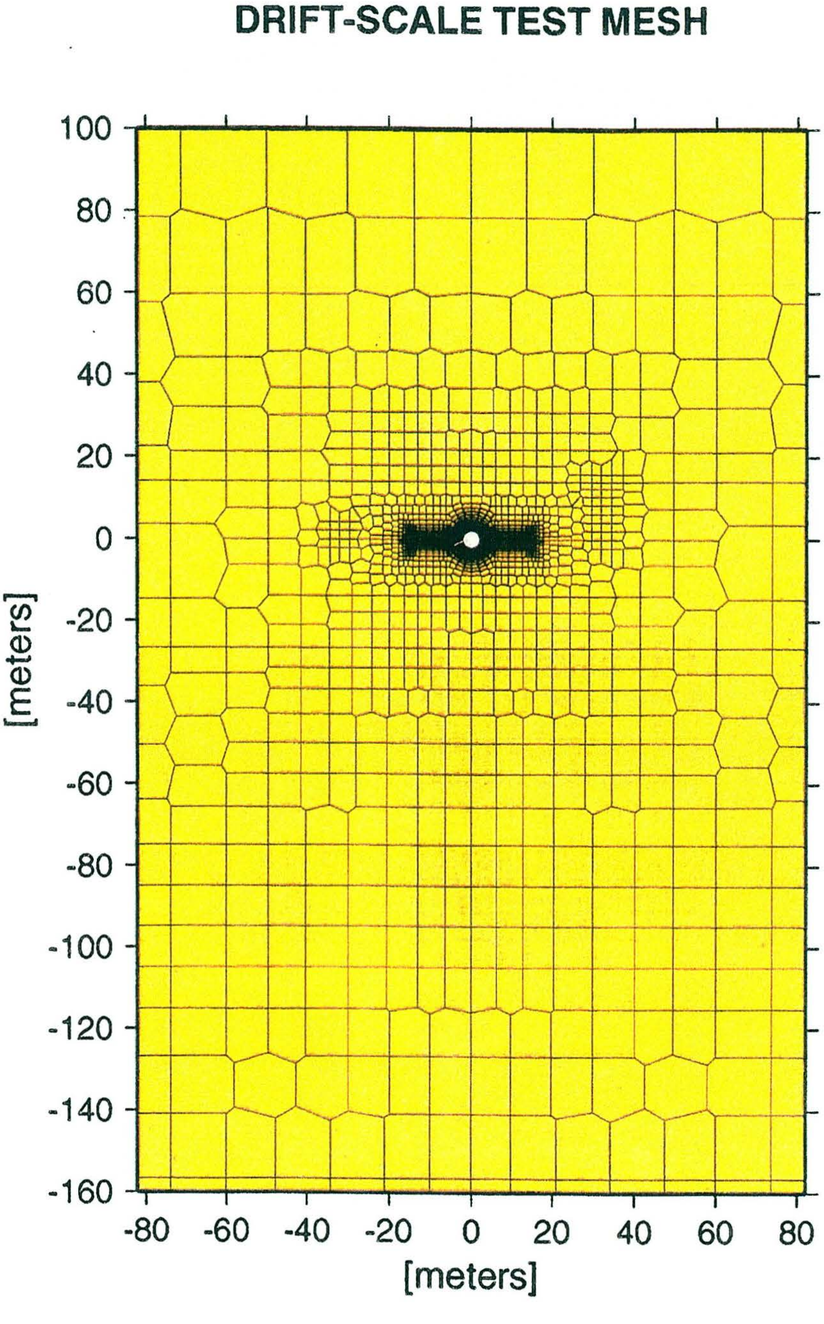

Figure 3.1a. Mesh used for thermo-hydro-chemical modeling of the drift scale heater test adopted from Birkholzer and Tsang [1997].

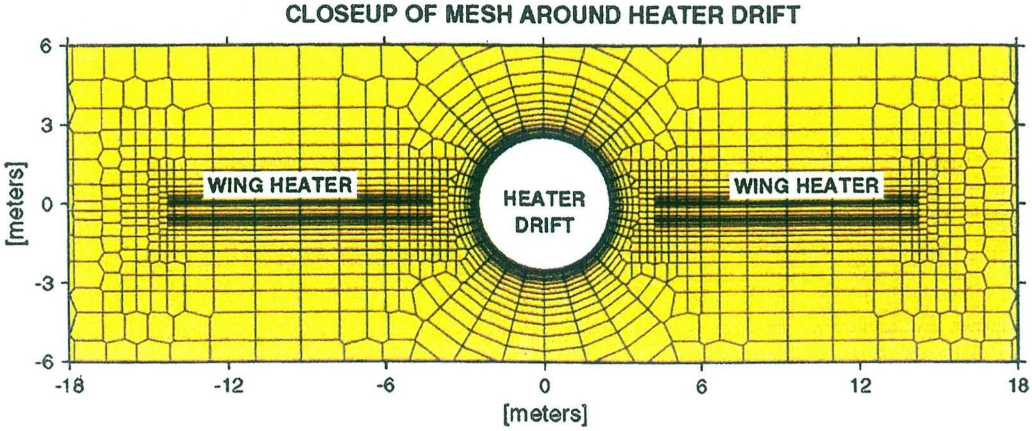

Figure 3.1b. Closeup view of region around central drift heater and wing heaters showing local grid refinement adopted from Birkholzer and Tsang [1997].

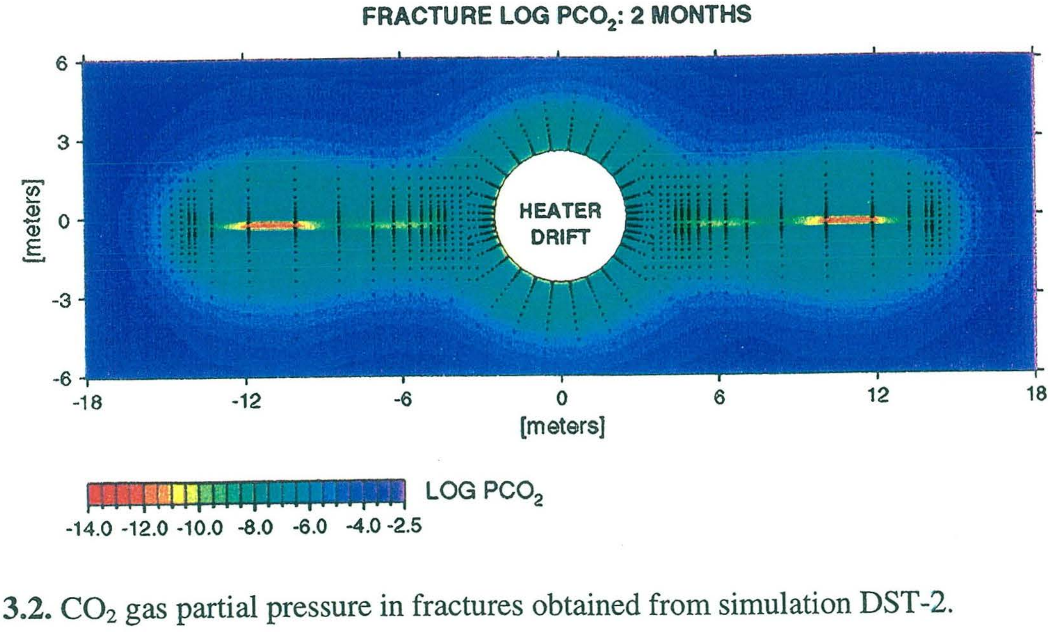

Figure 3.2. CO_2 gas partial pressure in fractures obtained from simulation DST-2.

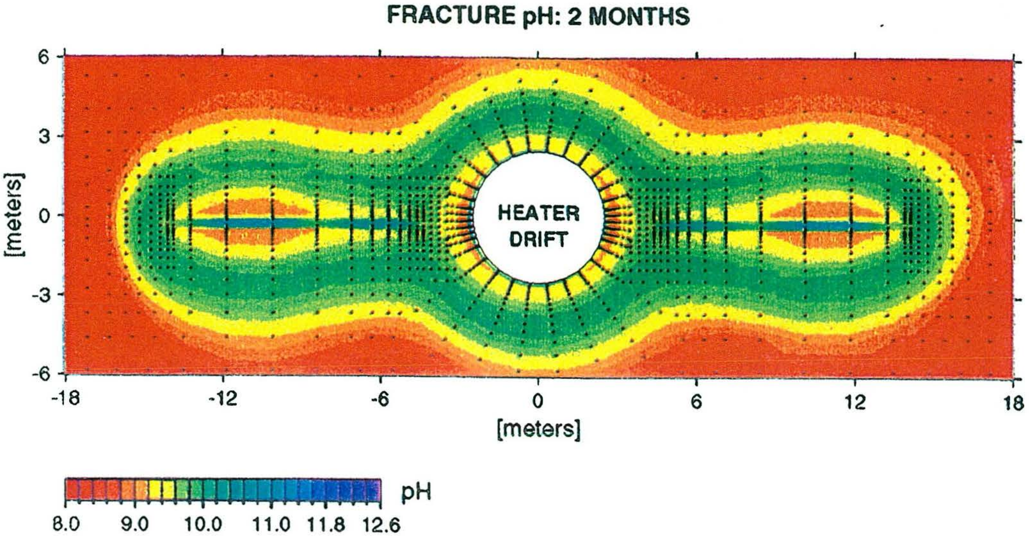

Figure 3.3. Pore water pH in fractures from simulation DST-2

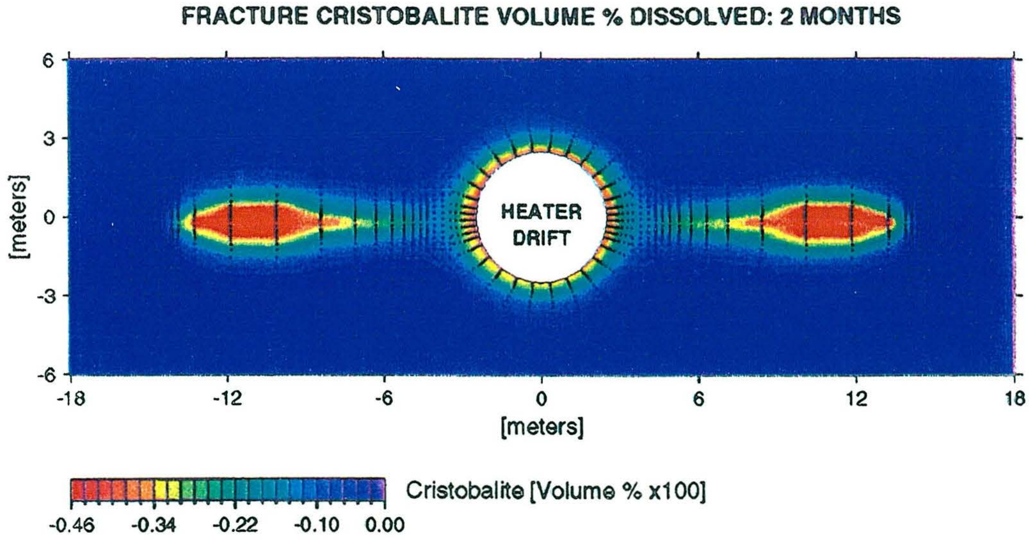

Figure 3.4. Volume percentage change of cristobalite in fractures from simulation DST-2

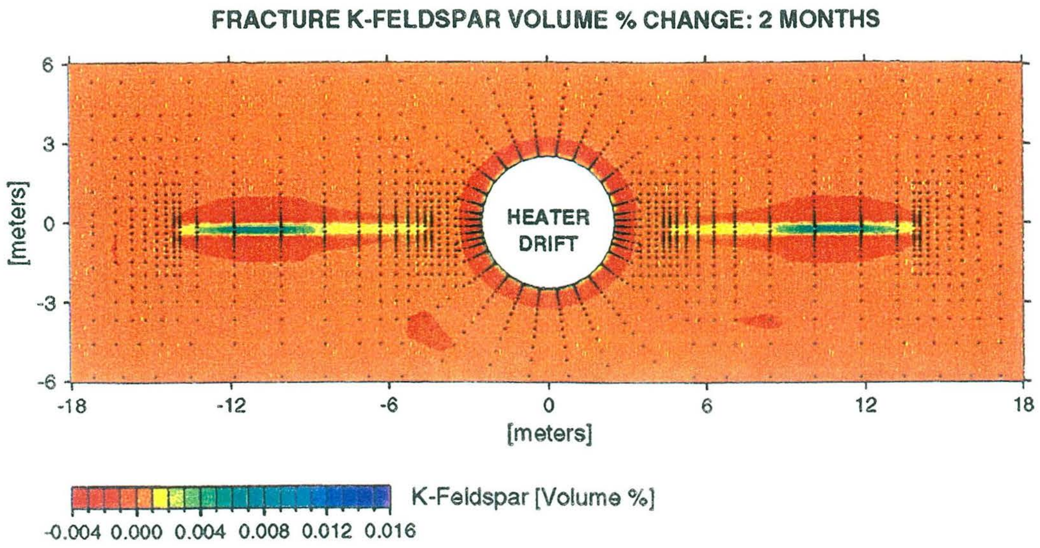

Figure 3.5. Volume percentage change of K-feldspar in fractures from simulation DST-2.

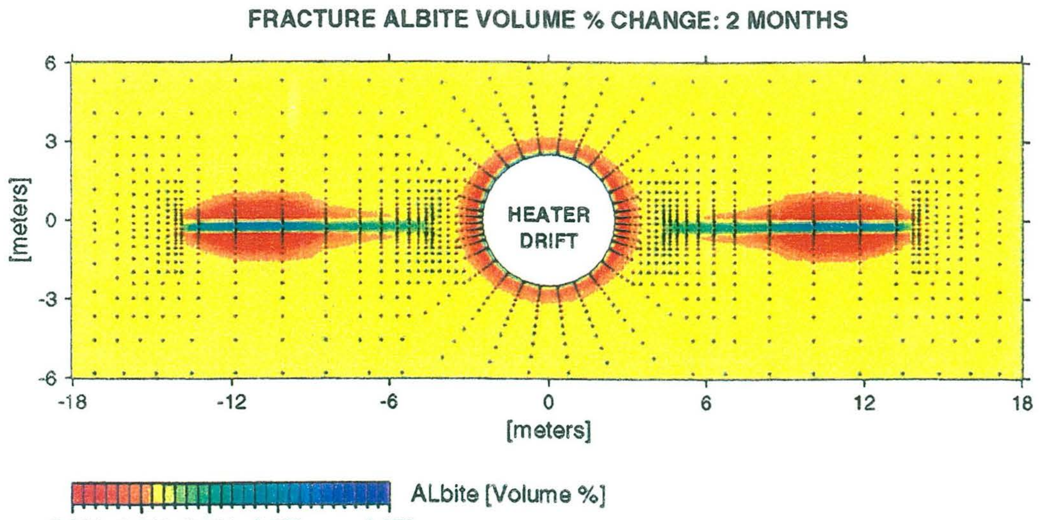

Figure 3.6. Volume percentage change of albite in fractures from simulation DST-2

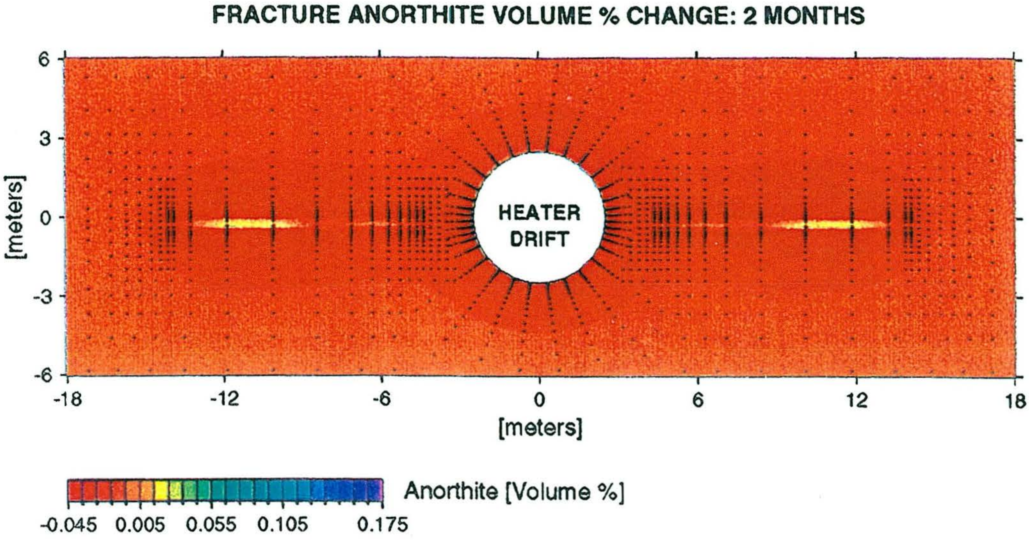

Figure 3.7. Volume percentage change of anorthite from simulation DST-2.

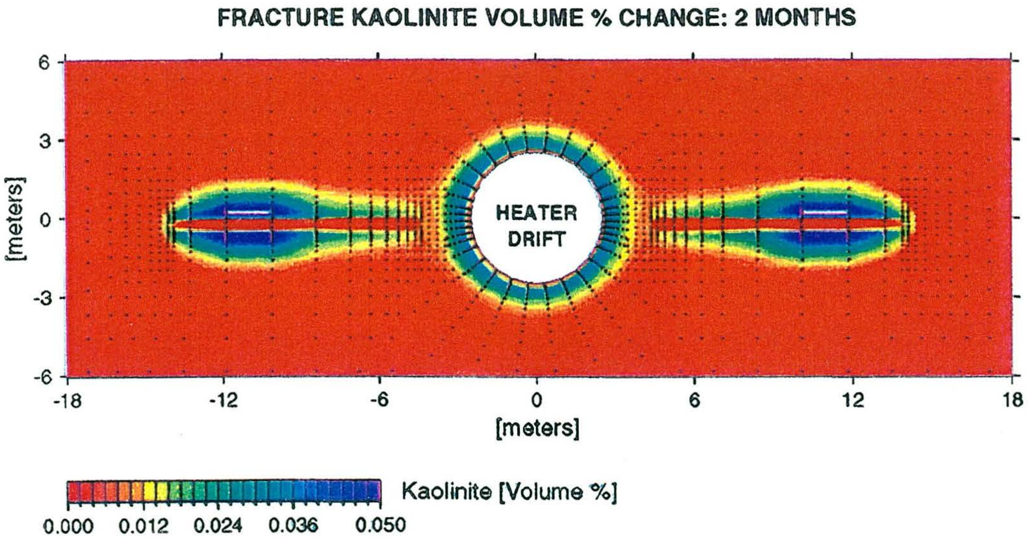

Figure 3.8. Volume percentage change of kaolinite from simulation DST-2

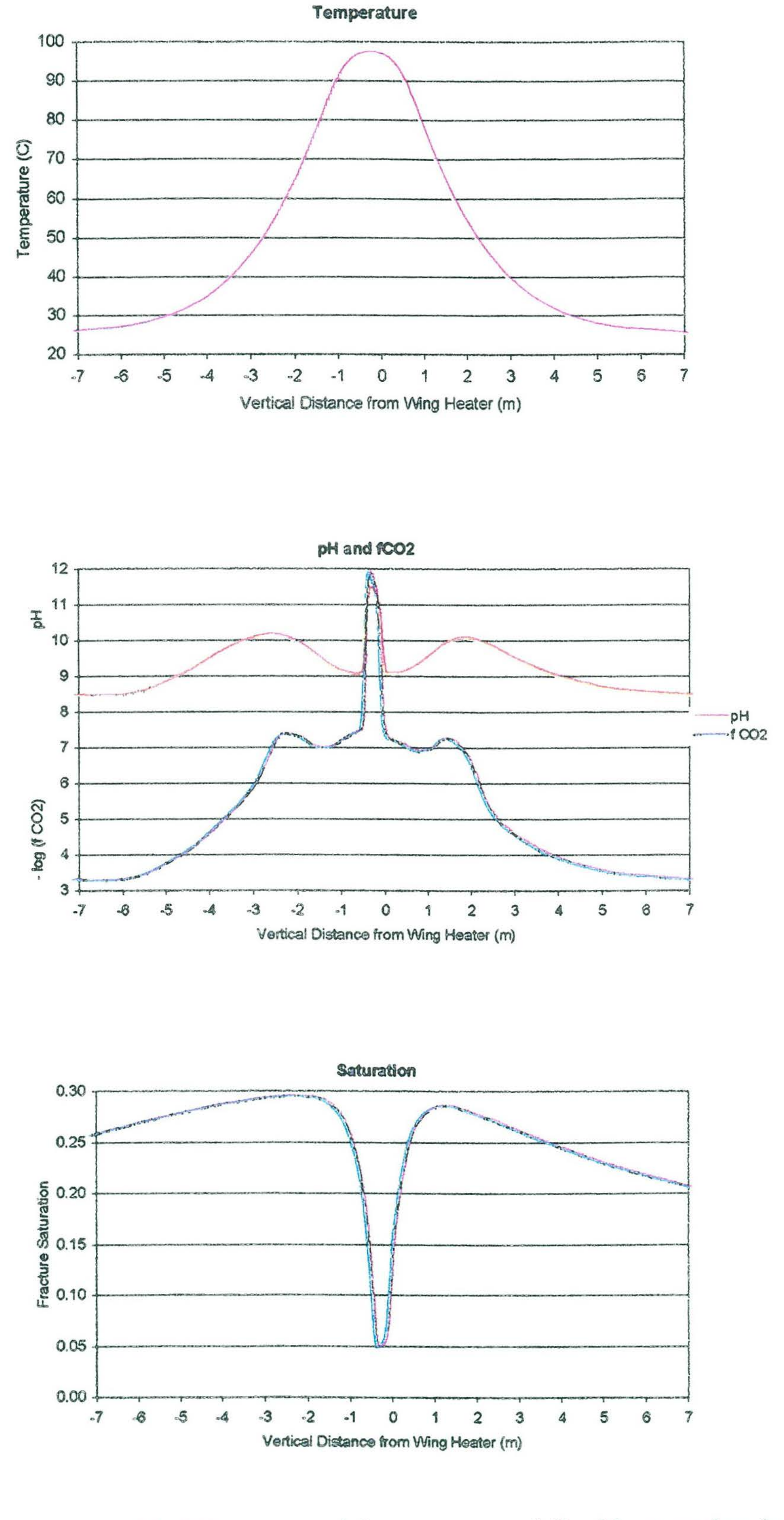

Figure 3.9. Temperature, pH, CO_2 gas partial pressure, and liquid saturation in fractures for a vertical profile through a wing heater (about 12 m to the left of the drift) from simulation DST-2

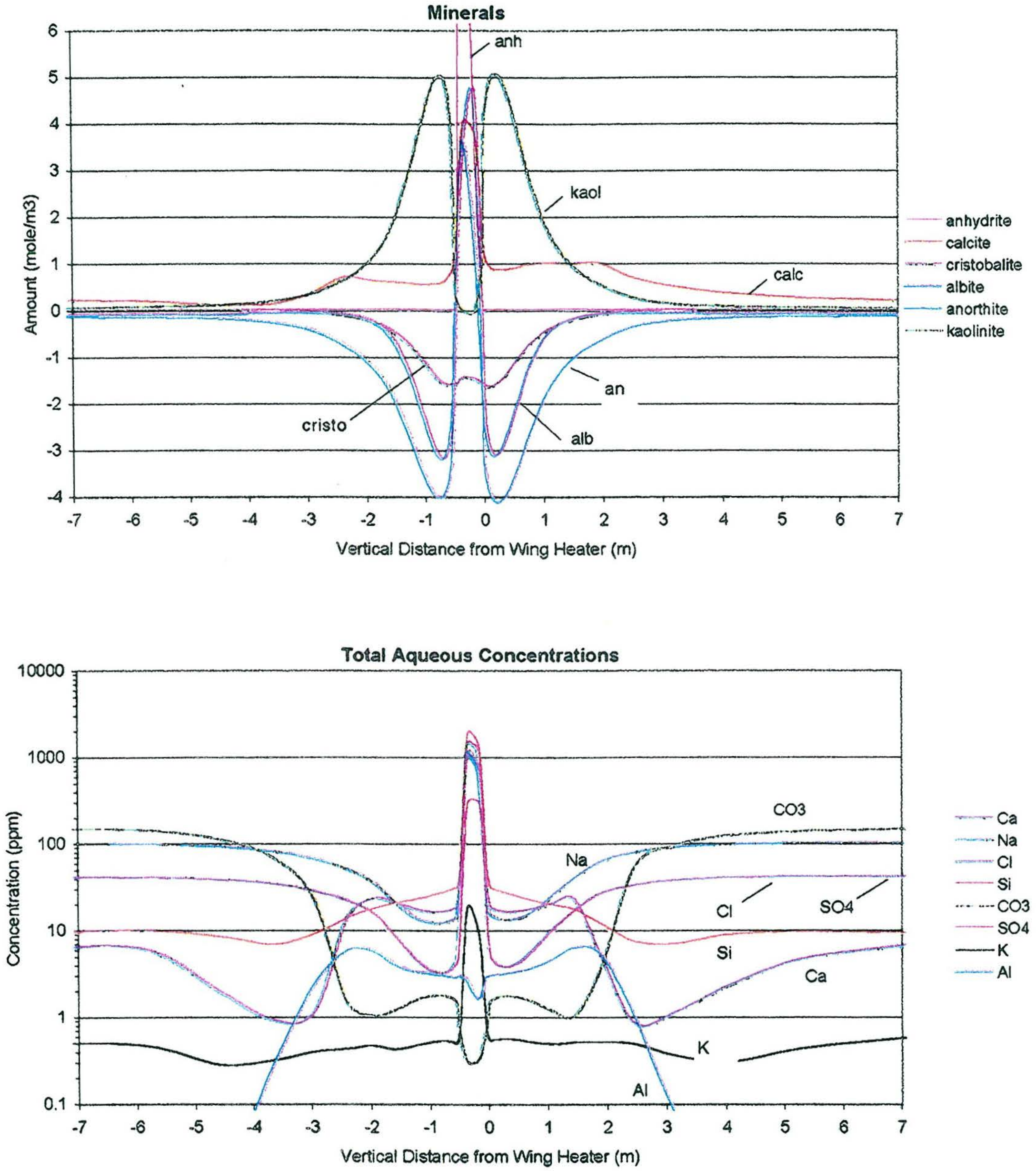

Figure 3.10. in fractures for a vertical profile through a wing heater (about 12 m to the left of the drift) from simulation DST-2

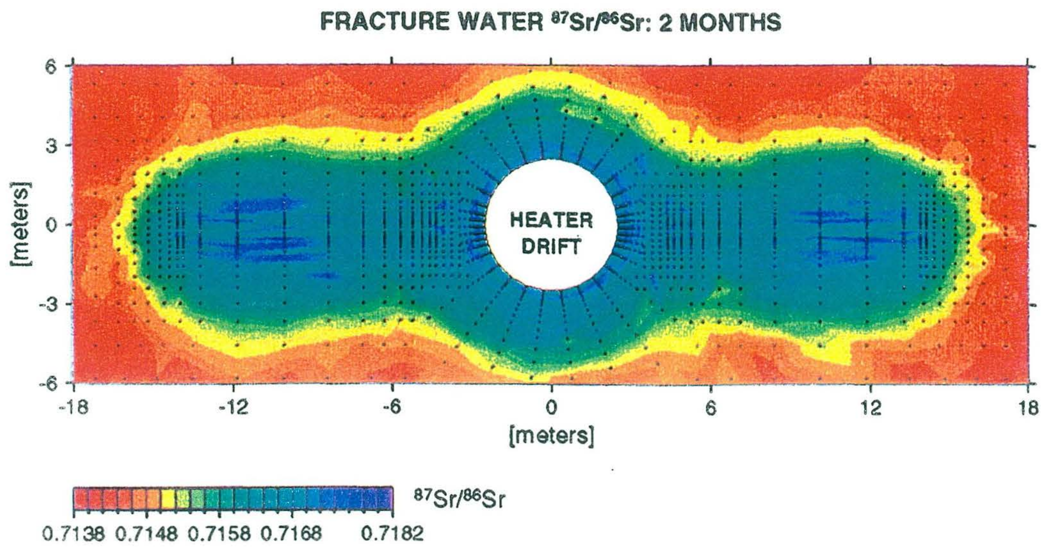

Figure 3.11. Pore water $^{87}S_r/^{86}S_r$ ratio in fractures from simulation DST-2.

4. Chemical evolution in irrigated soil.

4.1 Problem statement

To demonstrate TOUGHREACT capabilities for ambient flow and reactive transport in unsaturated porous media, chemical evolution in an irrigated soil was simulated. Variation of CO_2 gas partial pressure plays an important role in the chemical evolution of unsaturated soils [*Domenico et al.*, 1990]. Elevated CO_2 pressures are due primarily to root and microbial respiration and, to lesser extent, the oxidation of organic matter [*Palmer and Cherry*, 1984]. According to these investigators, value for soils range generally from the atmospheric partial pressure, 3.5×10^{-4} bar, to maximum values more than 500 times larger. We did not attempt to model the complexity of CO_2 production in the unsaturated zones, but simply assumed a fixed linear partial pressure distribution from the atmospheric value at the soil surface to 0.09 bar at the bottom of the domain. Calcite dissolution/precipitation and cation exchange are also modeled for the soil-water interaction. The displacement of exchanged Na by Ca is significant for evaluating irrigation water quality [*Simunek and Suares*. 1994].

4.2. Hydrogeochemical system

In this example, a drip irrigation at the soil surface is considered. The irrigation devices are assumed to be located at 1 m spacing. Because of the symmetry of the flow and transport fields, only the part of the profile between an irrigation device and the midpoint distance to the next device needs to be simulated. A depth of 0.75 m and a width of 0.5 m are considered (see Figure 4.1). A constant grid spacing of 0.05 m is used for both directions. Free drainage is used as the bottom boundary condition. An irrigation water flux of 2.32×10^{-7} m^3/m is applied to the left-top grid block of the discretized domain. A zero flux is specified at the left and right boundaries as well as the portion of the upper boundary not flooded with water. The initial water saturation is 0.4 for the whole domain. The saturated permeability is 7×10^{-13} m/s. The *van Genuchten's* [1980] retention curve and relative hydraulic conductivity function are used with the following parameters: $\lambda=0.372$, $S_{lr}=0.03$, $S_{ls}=1$, and $P_0=6.66\times10^3$ Pa. The soil grain density is 2600 kg/m^3.

As infiltration water moves downwards, it rapidly dissolves CO_2, which occurs in soil gas at partial pressures much larger than the atmospheric value. Calcite is present in the soil profile with a volume fraction of 0.05. Initially, the soil solution has a slightly sodic chemical composition with total dissolved concentrations Na = 7.5×10^{-3}, Ca = 3.9×10^{-6}, Mg = 1.0×10^{-6}, K = 1.0×10^{-6}, C = 7.5×10^{-3}, Cl = 7.5×10^{-3}, $SO_2^{2-} = 7.5\times10^{-3}$ mol/l and pH = 6.3. The cation exchange capacity (CEC) is equal to 95 meq/l. Most of the exchange positions are initially occupied by Na. Dissolved concentrations are modified after equilibrium with a partial pressure of CO_2, calcite and exchanged sites, according to which initial water composition for the simulation varied with depth due to variation of CO_2 partial pressure. The irrigation water composition is taken from a calcite under-saturated Colorado river water from the Grand Valley with total dissolved concentrations Na = 2.55×10^{-3}, Ca = 2.63×10^{-3}, Mg = 1.05×10^{-3}, K = 6.0×10^{-5}, C = 2.33×10^{-3}, Cl = 1.94×10^{-3}, SO_2^{2-} = 2.03×10^{-3} mol/l, and pH = 7 [*Simunek and Suares*, 1994]. The chemical reactions considered are show in Table 4.1. The Gaines-Thomas convention [*Appelo and Postma*, 1993] was used for cation exchange. In this convention, exchanged cation activities are calculated by using the equivalent fraction of the exchanged cations. All reactions are assumed to proceed at equilibrium. Chemical calculations are carried out at a constant temperature of 25 °C.

Table 4.1. List of chemical reactions considered for the irrigated soil. Equilibrium constants for cation exchange (selectivities) are taken from *Appelo and Postma*. [1993] and the others are from the EQ3/6 database [*Wolery*, 1992].

Geochemical reactions	$\log_{10}(K)$ at 25 °C
Aqueous dissociation:	
$OH^- = H_2O - H^+$	13.995
$CO_3^{2-} = HCO_{4-} + H^+$	10.329
$CO_2(aq) = HCO_{4-} + H^+ - H_2O$	-6.3447
$CaHCO_3^+ = Ca^{2+} + HCO_{4-}$	-1.0467
$CaCO_3(aq) = Ca^{2+} + HCO_{4-} - H^+$	7.0017
$MgHCO_3^+ = Mg^{2+} + HCO_{4-}$	-1.0357
$MgCO_3(aq) = Ca^{2+} + HCO_{4-} - H^+$	7.3499
$NaHCO_3(aq) = Na^+ + HCO_{4-}$	-0.1541
$CaSO_4(aq) = Ca^{2+} + SO_4^{2-}$	-2.1111
$NaSO_4^- = Na^+ + SO_4^{2-}$	-0.082
Cation exchange:	
$Na^+ + 0.5Ca\text{-}X_2 = 0.5Ca^{2+} + Na\text{-}X$	0.38
$Na^+ + 0.5Mg\text{-}X_2 = 0.5Mg^{2+} + Na\text{-}X$	0.50
$Na^+ + K\text{-}X = K^+ + Na\text{-}X$	0.20
Gas dissolution:	
$CO_2(g) = HCO_{4-} + H^+ - H_2O$	-7.8136
Mineral dissolution:	
Calcite $= Ca^{2+} + HCO_{4-} - H^+$	1.8487

4.3. Results

Initially, water pressure in the soil is constant with depth so that, at t = 0, the flow is driven purely by gravity with a unit downward hydraulic gradient. Water infiltrates into the soil and its moisture content increases. To facilitate the analysis of the spatial distribution and time evolution of water saturation and various chemical species, 2-D contour plots at some selected times and graphs showing the variation of concentrations along the left under the drip flood grid blocks are presented. From Figure 4.1, it can be seen that the saturation front propagates gradually. A steady-state water saturation profile is reached after approximately 5 days. To display solute transport, the concentration distribution of the conservative species Cl^- is presented in Figure 4.2.

Irrigation water has a very low dissolved inorganic carbon concentration of 2.33×10^{-3} mol/l. This water mixing with the interstitial water at the top of the model domain is still not in equilibrium with respect to CO_2(g) and calcite which cause their dissolution (see Figure 4.3 and Figure 4.4). At this point calcite dissolution (130 moles per cubic meter medium or mol/m^3 after 30 days) is larger than CO_2(g) dissolution (28 mol/m^3). Dissolution of one mole calcite consumes one mole H^+, while dissolution of one mole CO_2(g) creates one mole H^+. The pH value increases since there is more dissolution of calcite than that of CO_2(g). In addition, the infiltration water has a low pH (7.0). The resulting pH reaches a value of 7.45 (see Figure 4.5b) which is a value between initial pH (8.15) and infiltration pH (7.0). As water moves downward to the second grid block, the dissolution pattern is changed. An increase in the CO_2 partial pressure results in strong dissolution of CO_2 at this point (see Figure 4.4b). The dissolution of calcite is much less than that at the top (see Figure 4.3b). Continuing downward, the dissolution patterns are similar to those at the second grid block. From both contour plots and graphs at the vertical cross-section we can observe that the peak values of calcite dissolution occur at the top due to the mixing effect, while gas dissolution peaks in the second grid block due to increasing CO_2 partial pressure. The general forms of pH distribution at the initial and final states are controlled by the CO_2 partial pressure; the higher this pressure, the lower the pH. This is why pH decreases from the top to the bottom. As time passes, the pH front propagates both downwards and to the right side of the domain. On the right side of the contour plot (Figure 4.5a) a residue of the initial pH pattern can be seen. The final pH curve is lower than the initial one everywhere, and in the lower part even lower than pH at the recharge water. This is caused by continuing dissolution of $CO_2(g)$ from the top to the bottom due to the depth dependent fixed partial pressure. This external amount of $CO_2(g)$ (equal to the dissolution, see Figure 4.4) is assumed to be provided by root and microbial respiration and organic matter oxidation [*Palmer and Cherry*, 1984].

Total dissolved inorganic carbon increases from the top to the bottom as the CO_2 partial pressure increases (see Figure 4.6). Although dissolution of $CO_2(g)$ and calcite results in an increase of total dissolved carbon, its concentration is still lower than the initial one due to extremely low concentrations in the irrigation water. The overall reactive transport front for the carbon lags behind the conservative transport (compare the position at 5 days in Figure 4.6b to the position at the same time in Figure 4.2b for Cl). Contrary to total carbon, dissolved calcium concentrations increase rather than decrease with depth (see Figure 4.7). Its concentration in the irrigation water (2.63×10^{-3} mol/l) is greater than its initial one. Calcite dissolution adds more calcium. Consequentially, Ca concentration increases gradually from the top to the bottom. Peak values are developed due to the dissolution.

Ca-Na exchange processes take place simultaneously, increasing the complexity of chemical evolution. Initially, most of exchange sites are occupied by Na (see Figure 4.9 for exchanged Ca and Figure 4.10 for exchanged Na). Transport and calcite dissolution processes provide significant dissolved Ca. As a result, Ca replaces Na on the exchanged complexes. The exchanged Ca also has a peak wave. Its position coincides with that of the corresponding dissolved Ca (compare Figure 4.9 to Figure 4.7). The loss of dissolved Ca is supplied by calcite dissolution according to equilibrium constraints. To maintain the constant total exchange sites, Na must release from the exchanged complex. This additional source for the dissolved Na due to the cation exchange (retardation effect) generates a slight peak (see the curve at 5 days and especially the contour plot in Figure 4.8). Mg and K also participate in the exchange processes. Since their concentrations at the initial and irrigation waters are very low, the influence is negligible.

4.4. Discussion

In unsaturated soils, variations of CO_2 gas partial pressure play a dominant role in the pH distribution. The higher this pressure, the lower the pH. As a result, aqueous and exchanged species concentrations are redistributed. The depth dependent fixed partial pressure distribution in our simulation is somewhat artificial. However, if CO_2 gas productions by root and microbial respiration and organic matter oxidation were known, TOUGHREACT could model the full coupled gas transport process. In addition, calcite dissolution and cation exchange processes also play a role in the chemical evolution. The example has demonstrated the capability of the model to deal with water flow and reactive transport under ambient conditions in variably saturated porous media.

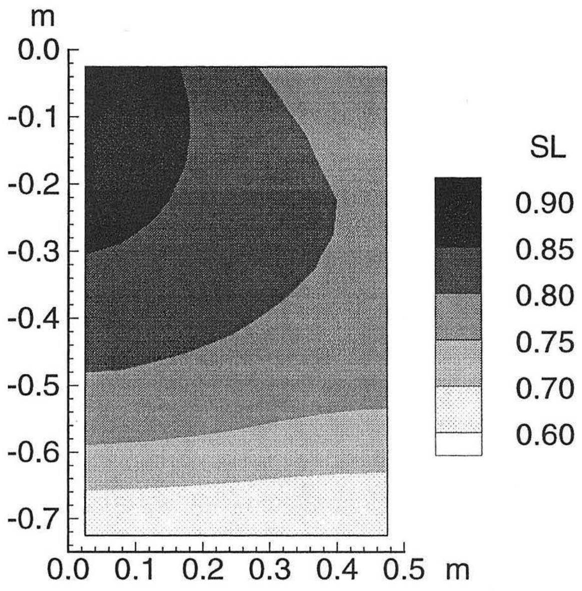

(a) Contour plot at 0.5 days

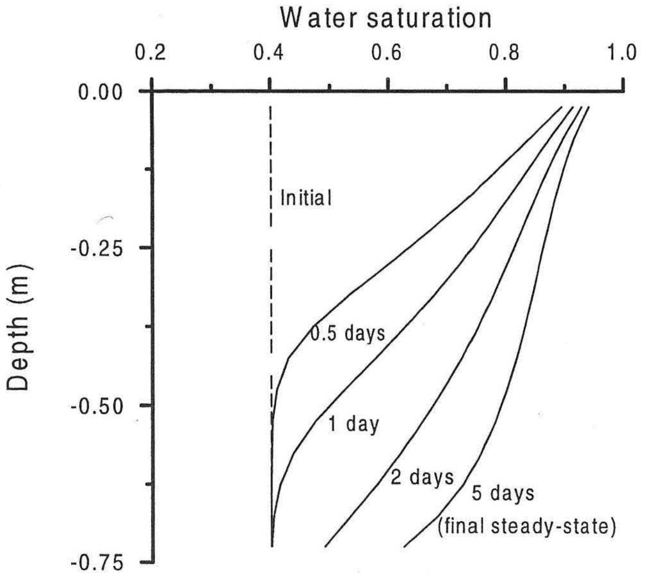

(b). Temporal evolution along the x=0 vertical cross-section

Figure 4.1. Water saturation distribution for the irrigation problem

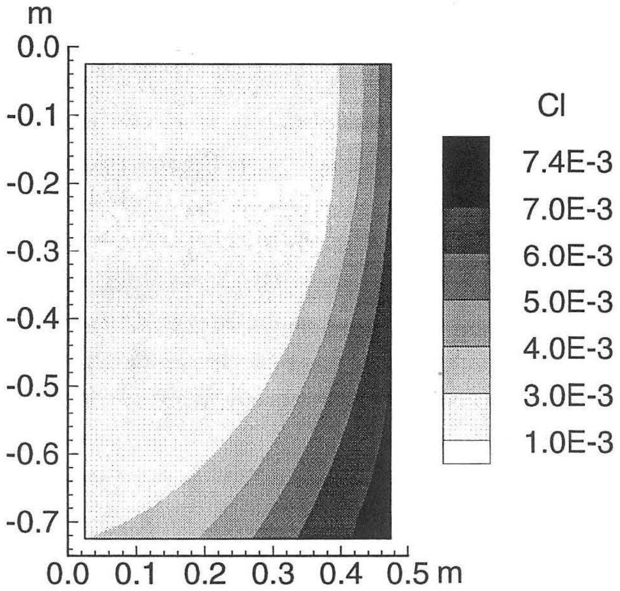

(a) Contour plot at 0.5 days

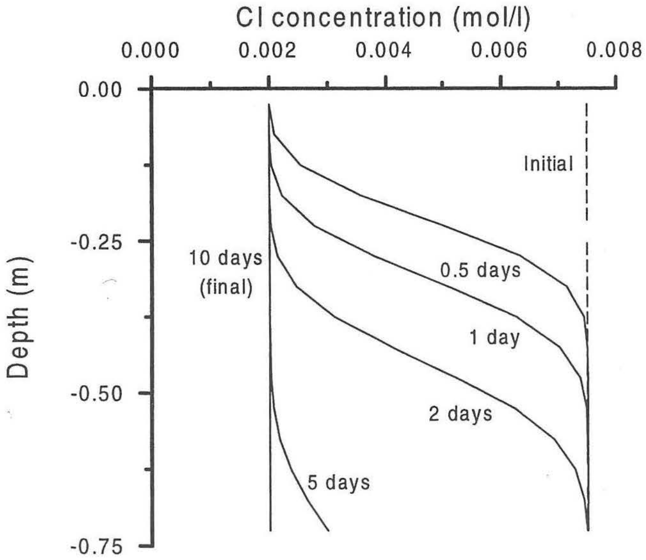

(b). Temporal evolution along the x=0 vertical cross-section

Figure 4.2. Cl concentration (mol/l) for the irrigation problem.

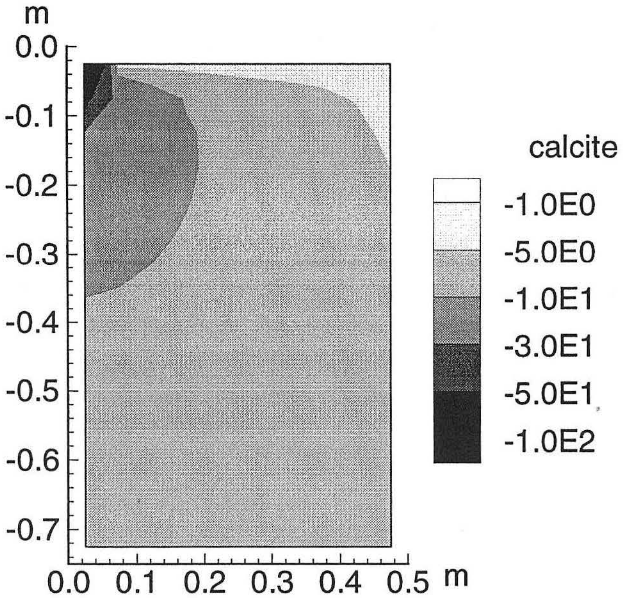

(a). Contour plot at 30 days (units: mol/m^3 or moles per cubic meter medium).

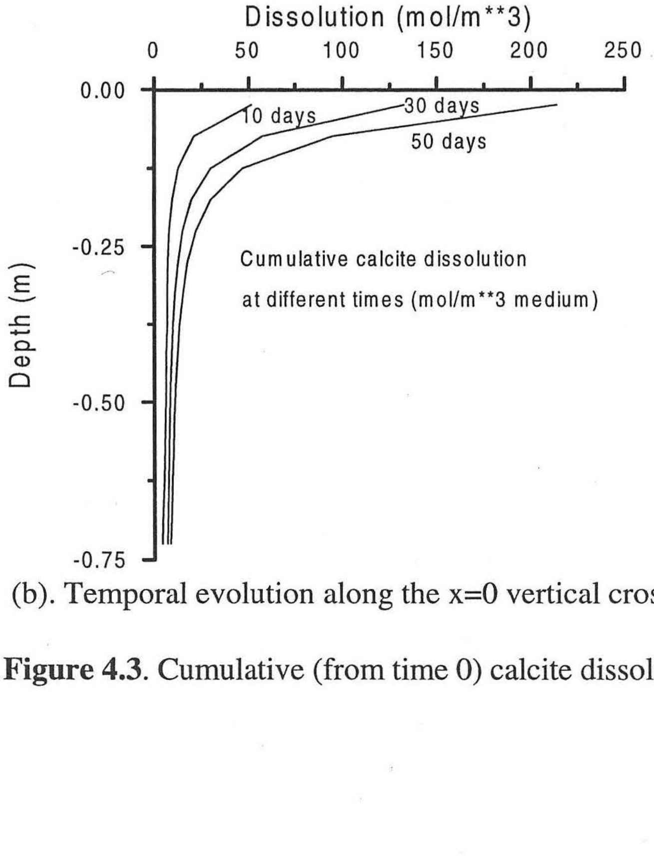

(b). Temporal evolution along the x=0 vertical cross-section

Figure 4.3. Cumulative (from time 0) calcite dissolution for the irrigation problem..

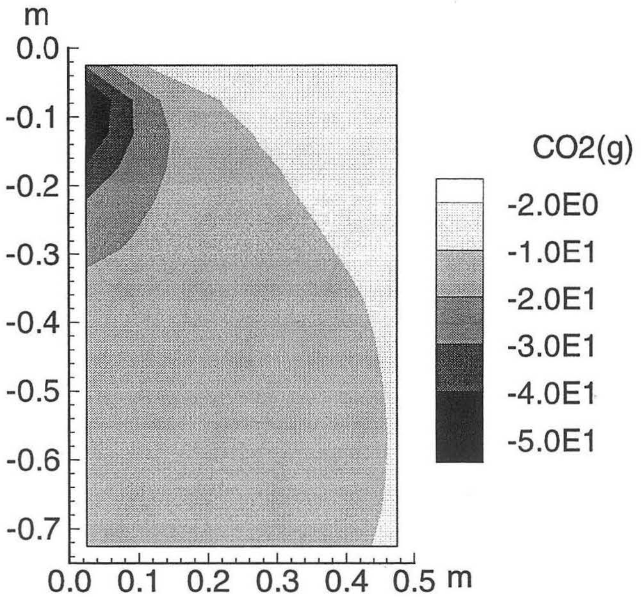

(a). Contour plot at 30 days (units: mol/m^3 or moles per cubic meter medium).

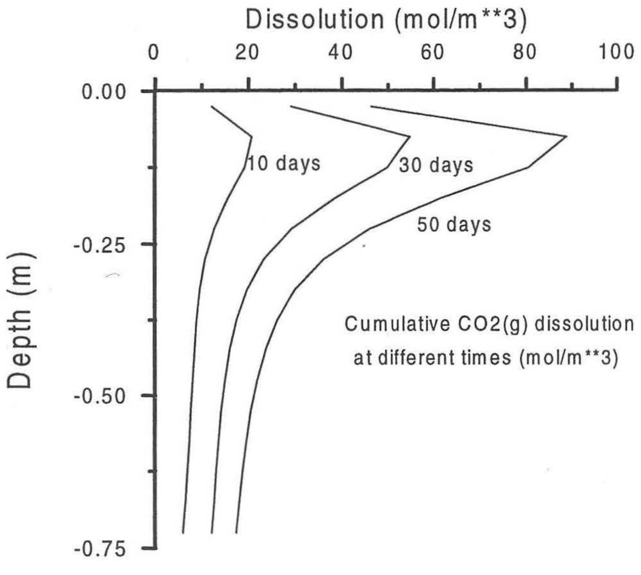

(b) Temporal evolution along the x=0 vertical cross-section

Figure 4.4. Cumulative (from time 0) CO_2 gas dissolution for the irrigation problem.

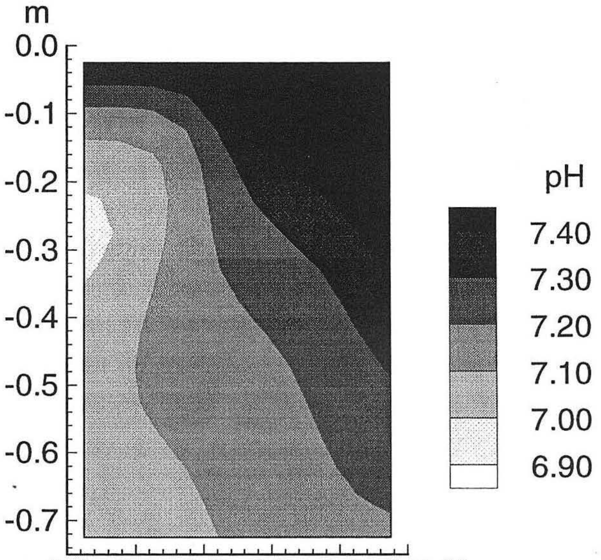

(a). Contour plot at 5 days

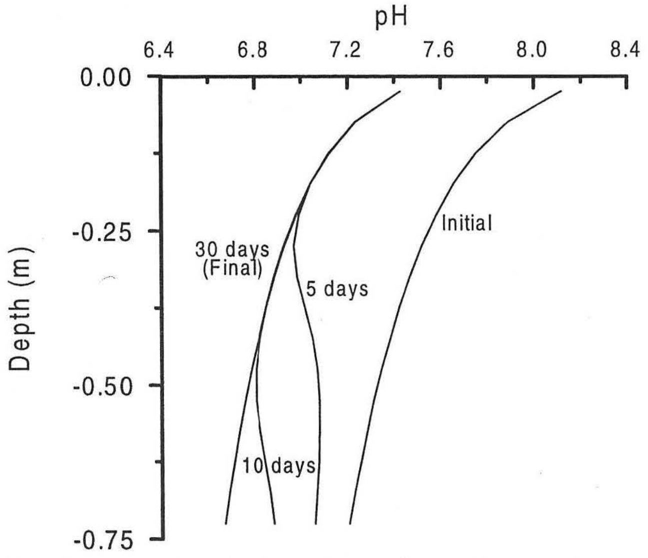

(b) Temporal evolution along the x=0 vertical cross-section

Figure 4.5. pH distribution for the irrigation problem.

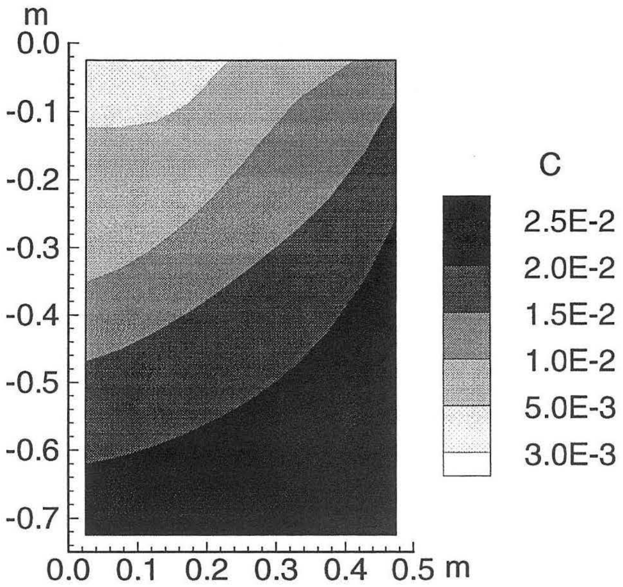

(a). Contour plot at 5 days (units: mol/l).

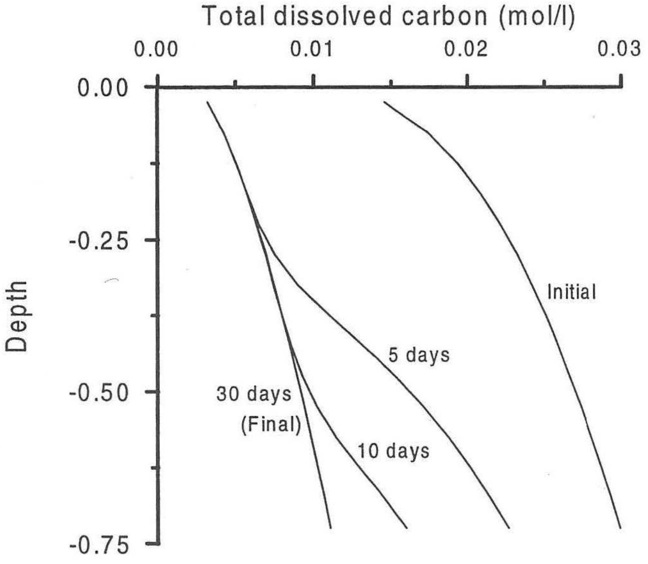

(b) Temporal evolution along the x=0 vertical cross-section.

Figure 4.6. Total dissolved carbon concentration (mol/l)for the irrigation problem.

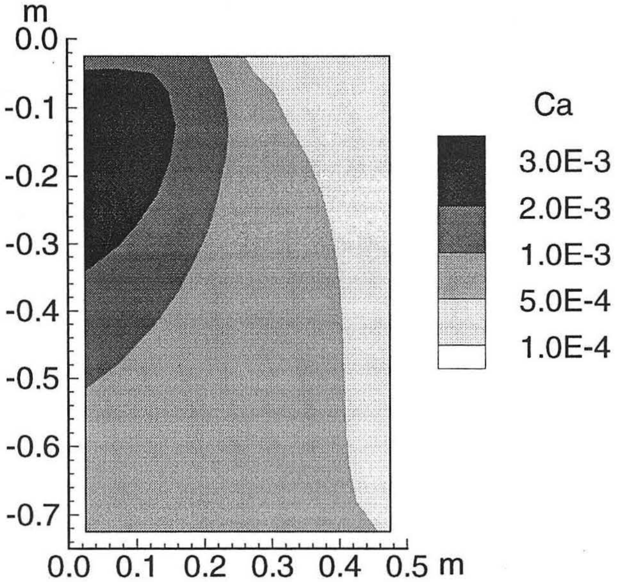

(a). Contour plot at 5 days (units: mol/l).

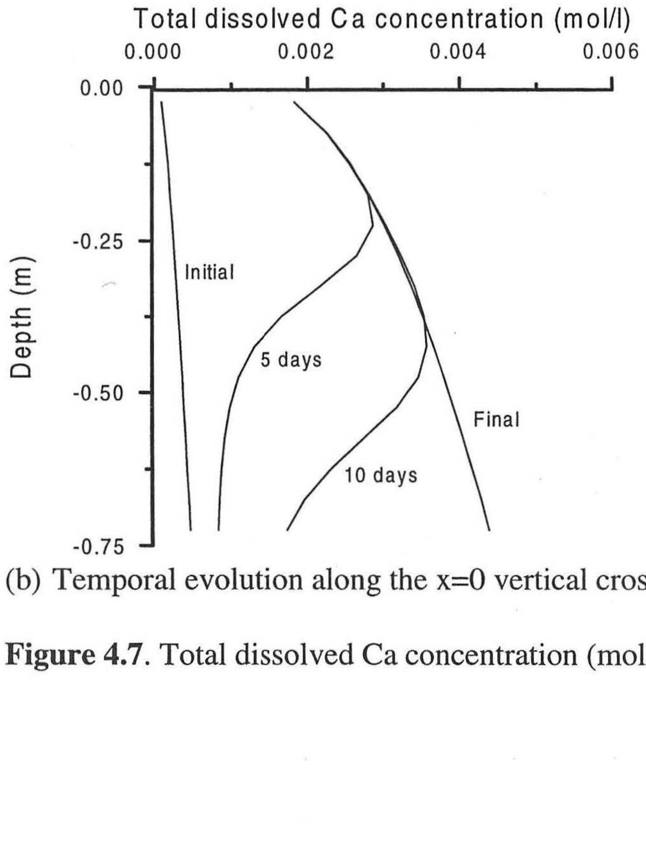

(b) Temporal evolution along the x=0 vertical cross-section.

Figure 4.7. Total dissolved Ca concentration (mol/l) for the irrigation problem.

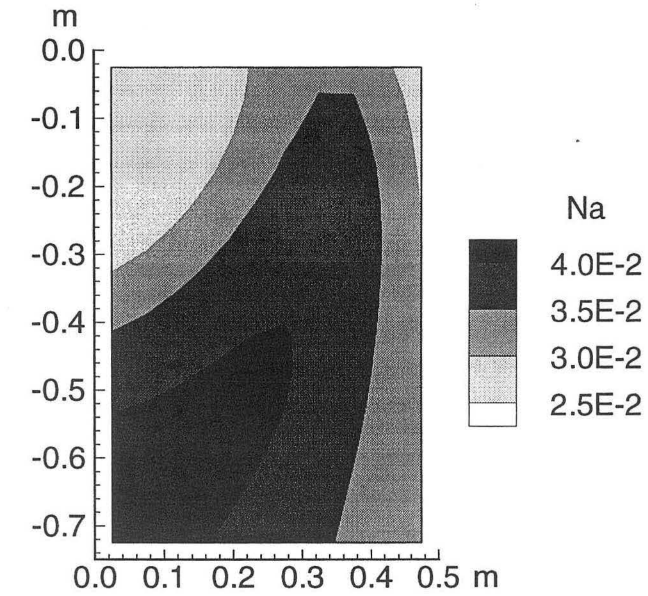

(a). Contour plot at 5 days (units: mol/l).

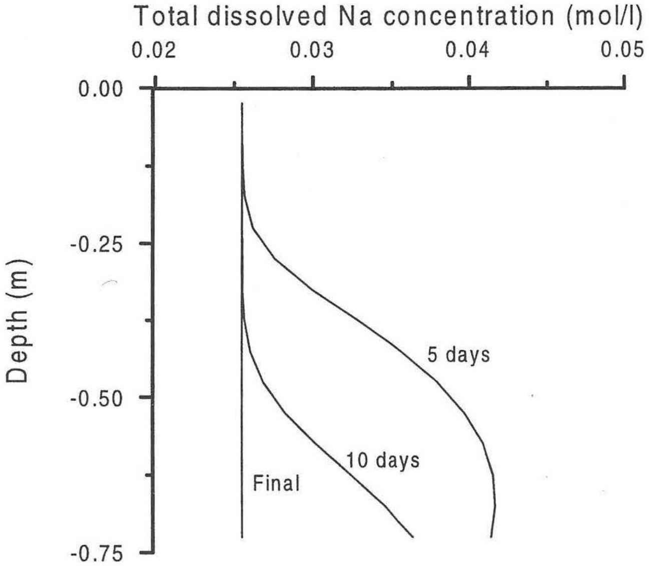

(b) Temporal evolution along the x=0 vertical cross-section.

Figure 4.8. Total dissolved Na concentration (mol/l) for the irrigation problem.

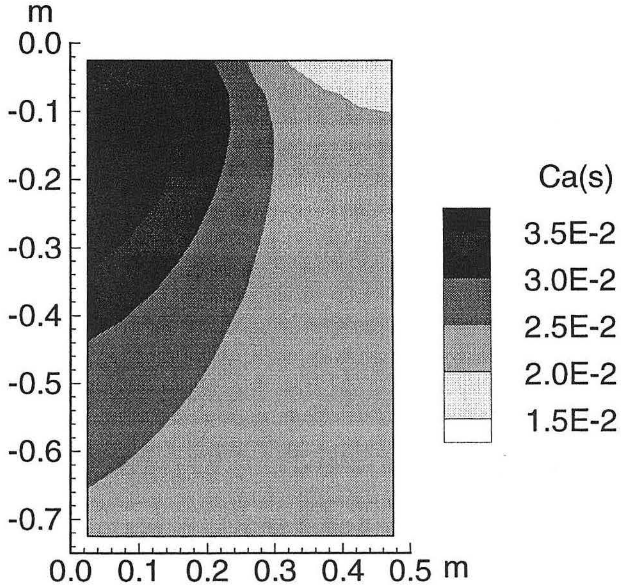

(a). Contour plot at 5 days (units: mol/l).

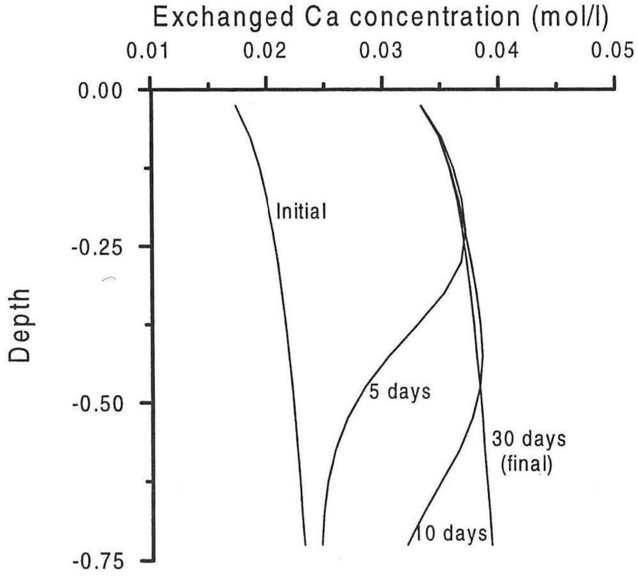

(b) Temporal evolution along the x=0 vertical cross-section.

Figure 4.9. Exchanged Ca concentration (mol/l) for the irrigation problem.

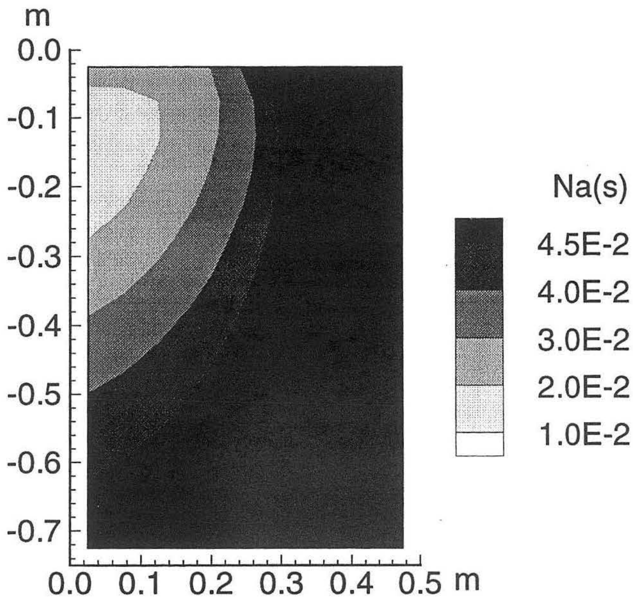

(a). Contour plot at 5 days (units: mol/l).

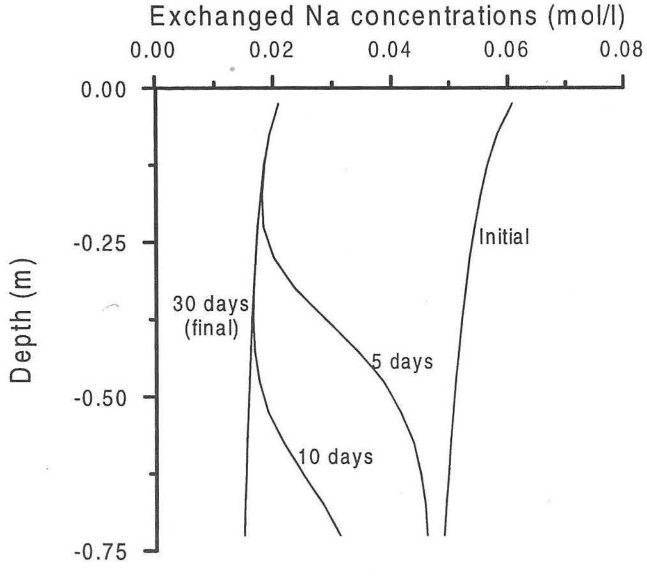

(b) Temporal evolution along the x=0 vertical cross-section.

Figure 4.10. Exchanged Na concentration (mol/l) for the irrigation problem.

5. Conclusions

Three applications covering a variety of reactive transport problems have been successfully simulated with the TOUGHREACT. The model is well suited for flow and reactive transport in variably saturated porous and fractured media. Heat driven fluid flow and effects on chemical reactions, and gaseous species transport and interaction with aqueous phase are major features of the model. Although only one- or two-dimensional domains are used in the presented examples, the model can be applied to three-dimensional systems in hydrologically and geochemically heterogeneous media. The capabilities of the model have been illustrated with a few examples. The full potential is yet to be explored in the future.

Acknowledgement

The authors appreciate stimulating discussions with John Apps, Frederic Gérard and Tom Wolery. This work was supported by the Laboratory Directed Research and Development Program of the Ernest Orlando Lawrence Berkeley National Laboratory, under Contract No. DE-AC03-76SF00098 with the U.S. Department of Energy; and by the Director, Office of Civilian Radioactive Waste Management, U.S. Department of Energy, through Memorandum Purchase Order EA9013MC5X between TRW Environmental Systems Inc., and the Ernest Orlando Lawrence Berkeley National Laboratory.

Reference

Aagaard, P., and H.C. Helgeson, Thermodynamic and kinetic constraints on reaction rates among minerals and aqueous solutions, 1. Theoretical considerations, *American Journal of Science*, 282, 237-285, 1982.

Ague, J. J., and G. H. Brimhall, Geochemical modeling of steady state and chemical reaction during supergene enrichment of porphyry copper deposits, *Econ. Geol.*, 84, 506-528, 1989.

Appelo, C. A. J., and D. Postma, Geochemistry, groundwater and pollution, 1993.

Appelo, C. A. J., Cation and proton exchange, pH variations and carbonate reactions in a freshening aquifer, *Water Resour. Res.*, 30(10), 2794-2805, 1994.

Bandurraga, T.M., and G.S. Bodvarsson, Calibrating matrix and fracture properties using inverse modeling, Chapter 6 of "Development and calibration of the three-dimensional site-scale unsaturated-zone model of Yucca Mountain, Nevada (Eds: G.S. Bodvarsson, T.M. Bandurraga, and Y.S. Wu.)", Yucca Mountain Site Characterization Project Milestone SP24UFM4. Lawrence Berkeley National Laboratory Report LBNL-40376, Berkeley, California, 1997.

Birkholzer, J.T., and Y.W. Tsang, Pretest analysis of the thermal-hydrological conditions of the ESF Drift Scale Test. Yucca Mountain Project Level 4 Milestone SP9322M4, Lawrence Berkeley National Laboratory, Berkeley, California, 1997.

Birkholzer, J.T., and Tsang, Interpretive analysis of the thermo-hydrological processes of the drift scale test, Chapter 2 of "Drift scale test progress report", Yucca Mountain Project Level 4 Milestone SP2930M4, Lawrence Berkeley National Laboratory, Berkeley, California, 1998.

Brimhall, G.H., C. N. Alpers, and A. B. Cunnigham, Analysis of supergene ore-forming processes and ground water solute transport using mass balance principles, Econ. Geol., v. 80, p. 1227-1256, 1985.

Domenico, P. A., and F. W. Schwartz, Physical and chemical hydrogeology, John Wiley and Sons, New York, 824 pp., 1990.

Faure, G, Principle of isotopic geology, New York, Wiley and Sons, p. 464., 1977.

Gérard, F., T. Xu, G. Brimhall, and K. Pruess, Modeling reactive chemical transport problems with the codes EQ3/6 and TRANQUI, Lawrence Berkeley Laboratory Report LBL-40505, Berkeley, California, 1997.

Millington, R. J., and J. P. Quirk, Permeability of porous solids, *Trans. Faraday Soc.*, 57, 1200-1207, 1961.

Moridis, G.J., J.A. Apps; and G.S. Bodvarsson, ^{14}C Data analysis using the UZ model, Chapter 18 of "The site-scale unsaturated zone model of Yucca Mountain, Nevada, for the Viability

Assessment (Eds.: G.S. Bodvarsson, T.M. Bandurraga, and Y.S. Wu, eds)", Yucca Mountain Project Level 4 Milestone SP24UFM4, Lawrence Berkeley National Laboratory Report LBNL-40376, Berkeley, California, 1997

Paces, J.B., B. D. Marshall, J.F. Whelan, L.A. Neymark, and Z.E. Peterman, Summary of subsurface calcite and opal deposits and estimates of the probable distribution and isotopic compositions of hydrogenic minerals along the east-west cross drift, Yucca Mountain, Nevada. U.S. Geological Survey Open File Report, DTN: GS980308315215.009 (Q), Denver, Colorado, 1998.

Pruess, K., and T. N. Narasimhan, A practical method for modeling fluid and heat flow in fractured porous media, *Society of Petroleum Engineers Journal*, 25(1), 14-26, February, 1985

Pruess, K, and T. Xu, Coupled modeling of non-isothermal multiphase flow, solute transport and reactive chemistry in porous and fractured media: 1. Model development and validation, *J. Geophys. Res.*, this issue, 1998.

Palmer, C. D., and J. A. Cherry, Geochemical evolution of groundwater in sequences of sedimentary rocks, *J. Hydrol.*, Vol. 75, p. 27-65, 1984

Simunek, J., and D. L. Suares, Two-dimensional transport model for variably saturated porous media with major ion chemistry, *Water Resour. Res.*, 30(4), 1115-1133, 1994.

Sonnenthal, E.L., C.F. Ahlers, and G.S. Bodvarsson, Fracture and fault properties for the UZ site-scale flow model, Chapter 7 of "The site-scale unsaturated zone model of Yucca Mountain, Nevada, for the Viability Assessment (Eds.: G.S. Bodvarsson, T.M. Bandurraga, and Y.S. Wu)". Yucca Mountain Site Characterization Project Milestone Report SP24UFM4, Lawrence Berkeley National Laboratory Report LBNL-40376, Berkeley, California, 1997.

Sonnenthal, E., N. Spycher, J.A. Apps, and A. Simmons, Thermo-hydro-chemical predictive analysis for the drift-scale heater test, Yucca Mountain Project Level 4 Milestone SPY289M4, Lawrence Berkeley National Laboratory Report, Berkeley, California, 1998.

Van Genuchten, M. T., A closed-form equation for predicting the hydraulic conductivity of unsaturated soils, *Soil Sci. Soc. Am. J.*, 44(5), 892-898, 1980.

Wolery, T. J., EQ3/6, a software package for geochemical modeling of aqueous systems: Package overview and installation guide (version 7.0), Lawrence Livermore National Laboratory, Report UCRL-MA-110662 PT I, Livermore, California, 1992.

Xu, T., K. Pruess and G. Brimhall, An improved equilibrium-kinetics speciation algorithm for redox reaction in variably saturated flow system, Lawrence Berkeley National Laboratory Report LBNL-41789 (also submitted to *Computers & Geosciences*), Berkeley, California, 1998.

Yang, I.C., G. W. Rattray, and P. Yu, Interpretations of chemical and isotopic data from boreholes in the unsaturated-zone at Yucca Mountain, Nevada, U. S. Geological Survey, Water-Resources Investigation Report-96-4058, Denver, Colorado, 1996.

ERNEST ORLANDO LAWRENCE BERKELEY NATIONAL LABORATORY
ONE CYCLOTRON ROAD | BERKELEY, CALIFORNIA 94720

Prepared for the U.S. Department of Energy under Contract No. DE-AC03-76SF00098